Accessory phase petrogenesis in relation to major phase assemblages in pelites from the Nelson contact aureole, southern British Columbia

H. S. TOMKINS* AND D. R. M. PATTISON
Department of Geology and Geophysics, University of Calgary, Calgary, AB T2N 1N4, Canada
(helen.tomkins@sci.monash.edu.au)

ABSTRACT　Monazite petrogenesis in the Nelson contact aureole is the result of allanite breakdown close to, but downgrade and therefore independent of, major phase isograds involving cordierite, andalusite and staurolite. The development of garnet downgrade of the staurolite and andalusite isograds does not appear to affect the onset of the allanite-to-monazite reaction but does affect the textural development of monazite. In lower pressure, garnet-absent rocks, allanite breakdown results in localized monazite growth as pseudomorphous clusters. In higher pressure, garnet-bearing rocks, allanite breakdown produces randomly distributed, lone grains of monazite with no textural relationship to the original reaction site. Fluids liberated from hydrous phases (chlorite, muscovite) during garnet formation may have acted as a flux to distribute light rare earth elements more widely within the rock upon allanite breakdown, preventing the localized formation of monazite pseudomorphs. Despite these textural differences, both types of monazite have very similar chemistry and an indistinguishable age by electron microprobe chemical dating (157 ± 6.4 Ma). This age range is within error of isotopic ages determined by others for the Nelson Batholith. Garnet from the garnet, staurolite and andalusite zones shows euhedral Y zoning typified by a high-Y core, low-Y collar and moderate-Y annulus, the latter ascribed to allanite breakdown during garnet growth in the garnet zone. The cause of the transition from high-Y core to low-Y collar, traditionally interpreted to be due to xenotime consumption, is unclear because of the ubiquitous presence of xenotime. Accessory phase geothermometry involving monazite, xenotime and garnet returns inconsistent results, suggesting calibration problems or a lack of equilibration between phases.

Key words: allanite; contact metamorphism; garnet; monazite; yttrium.

INTRODUCTION

Monazite in metamorphic rocks has been shown to not only be a useful geochronometer, but also a sensitive and robust chemical recorder of prograde metamorphic processes and reactions (e.g. Foster *et al.*, 2002; Pyle & Spear, 2003; Kohn & Malloy, 2004). Through examination of compositional zoning and associated age domains in monazite grains, specific metamorphic reactions can be tied to specific ages, giving accuracy and detail to derived *P–T–t* paths. However the nature of the interaction between monazite (a phosphate), and coexisting rock-forming phases (mostly silicates), is complex and only beginning to be understood. The majority of work in this area has involved the establishment of chemical and petrogenetic links between monazite and garnet. Garnet is a particularly useful mineral when trying to link accessory and major phase equilibria due to its prevalence in metapelitic rocks, its involvement in a large number of the thermobarome-

ters used in metamorphic petrology, and its strong influence on the heavy rare earth element (HREE) and high field strength element budgets of any rock in which it occurs. In particular, garnet and monazite both incorporate significant Y, upon which many garnet–monazite petrogenetic interpretations have been based (Foster *et al.*, 2002; Pyle & Spear, 2003; Kohn & Malloy, 2004; Yang & Pattison, 2006).

For example, Pyle & Spear (2003) described four generations of monazite growth in pelites from New Hampshire (USA). Two of these generations were interpreted to have formed from garnet breakdown (zones 3 and 4), and one from xenotime breakdown in equilibrium with garnet, based on the Y composition of the monazite. Kohn & Malloy (2004) attributed significant monazite formation to garnet breakdown at the staurolite-in isograd in schists of the Great Smoky Mountains, North Carolina, with a corresponding increase in the Y content of monazite. They suggested that garnet and plagioclase supplied the phosphorous (P) for new monazite growth, with light rare earth elements (LREEs) sourced from sheet silicates and/or plagioclase, without any (or minimal) involvement of

*Present address: School of Geosciences, Monash University, Clayton, VIC, 3800, Australia.

additional accessory phases such as xenotime, apatite or allanite. Yang & Pattison (2006) performed a mass balance analysis of similar rocks from the Black Hills, North Dakota, and found that the amount of LREE in the silicates was insufficient for monazite formation by this process, and that there was no evidence for significant participation of garnet in the staurolite-forming reaction; rather, they ascribed monazite formation to allanite breakdown.

Foster et al. (2002) also described Y-rich monazite rims which they ascribed to garnet breakdown during retrogression and decompression. This phenomenon has also been described for zircon formation as a result of Zr-bearing garnet breakdown to cordierite during decompression in high-grade rocks from East Antarctica and SW Norway (Fraser et al., 1997; Degeling et al., 2001; Tomkins et al., 2005).

In contrast, Smith & Barreiro (1990) described a sequence of reactions in which detrital monazite broke down in the biotite zone to form allanite, followed upgrade at the staurolite-in isograd by metamorphic monazite formation, possibly involving the breakdown of allanite to form uranothorite as an intermediate step to monazite growth. Because the key reactants proposed in their study were other accessory phases (detrital monazite, allanite, xenotime and uranothorite), rather than rock-forming silicates, the association of monazite growth with the staurolite-in isograd was not considered to have been causative. In a similar study, Kingsbury et al. (1993) recognized significant monazite growth in the vicinity of the staurolite-in isograd. In the absence of allanite, they invoked various Th and Ce oxides and a Ce-poor phosphate as precursor phases to monazite.

Wing et al. (2003) documented breakdown of pre-existing monazite (detrital cores with low-grade metamorphic rims) to form euhedral allanite at the biotite isograd. Upgrade, at the onset of the aluminosilicate zone (andalusite or kyanite in this case, although the authors suggested that other Al-rich minerals such as staurolite or cordierite could play the same role) allanite disappeared to be replaced by metamorphic monazite. Wing et al. (2003) wrote reactions involving both accessory phases and rock-forming silicates to account for monazite growth at the Al_2SiO_5 isograd. In contrast, garnet formation at lower grade was not considered to have contributed to either monazite formation or dissolution.

Fraser et al. (2004) described monazite formation in the Ballachulish contact aureole of the Scottish Highlands. Without being able to identify any precursor phases in thin section, they suggested that monazite formed pseudomorphous clusters after either allanite or apatite in the vicinity of the cordierite-in (chlorite-out) isograd. Such clusters were also described by Wing et al. (2003), who interpreted them as the reaction products of euhedral allanite porphyroblasts.

The above overview demonstrates the diversity of interpretations of the contribution of accessory v. major silicate phases in the formation of monazite in pelitic metamorphic rocks. In an attempt to address this issue, monazite formation in contrasting prograde sequences from the Nelson contact aureole in southern BC has been studied to compare accessory mineral response to differing coexisting major phase assemblages. The aureole is ideal for such a study because it contains contrasting prograde silicate mineral assemblage sequences developed in monotonous graphitic argillites of the same stratigraphic unit, a situation ascribed to post-metamorphic tilting of the aureole (Pattison & Vogl, 2005). These include low-pressure cordierite-bearing, intermediate pressure andalusite-bearing and highest pressure staurolite-bearing sequences across a similar temperature range, with garnet additionally present in some of the intermediate pressure rocks and all of the highest pressure rocks.

GEOLOGY OF THE NELSON CONTACT AUREOLE

The Nelson contact aureole surrounds the Jurassic Nelson Batholith in south-eastern British Columbia, Canada (Fig. 1). The batholith is a composite intrusion with a broad main body extending southward into an elongate 'tail'. The Nelson Batholith is emplaced in regionally metamorphosed Upper Triassic to Early Jurassic metasedimentary rocks of the Slocan and Ymir Groups, which are thought to be correlative (Little, 1960). Both metasedimentary units have similar characteristics and are fairly uniform in lithology and composition, consisting of fine-grained graphitic and sulphide-rich shales and slates with rare sandy lenses. Prior to intrusion of the Nelson Batholith, the host rocks were regionally metamorphosed to chlorite-biotite grade (upper greenschist facies) in the early Jurassic.

The batholith and contact aureole are bounded to the west by the Eocene Slocan Lake-Champion Lakes fault system (Fig. 1), a major east-dipping normal fault zone (Carr et al., 1987). To the east the batholith and aureole are bounded by the Ainsworth Faults in the north-east and the Midge Creek Fault in the east and south-east, both normal, westerly dipping discontinuities (Fyles, 1967). The interior of this north–south trending fault block shows undisturbed intrusion–country rock relationships.

Geochronology in the area has focused on the batholith itself, with the age of regional metamorphism deduced from regional-scale correlations. Ages from K-Ar dating of biotite and hornblende (Nguyen et al., 1968) and U-Pb dating of zircon (Sevigny & Parrish, 1993) from the batholith are c. 160 and 158.9 ± 0.6 Ma, respectively. Further U-Pb zircon geochronology (Ghosh, 1995) gave ages ranging from 172 to 161 Ma, with an age of 160 Ma suggested for the tail. Following emplacement, a combination of Cretaceous-Palaeocene eastward thrusting and Eocene extension lead to uplift and tilting of the batholith (Archibald et al., 1983, 1984; Carr et al., 1987; Parrish
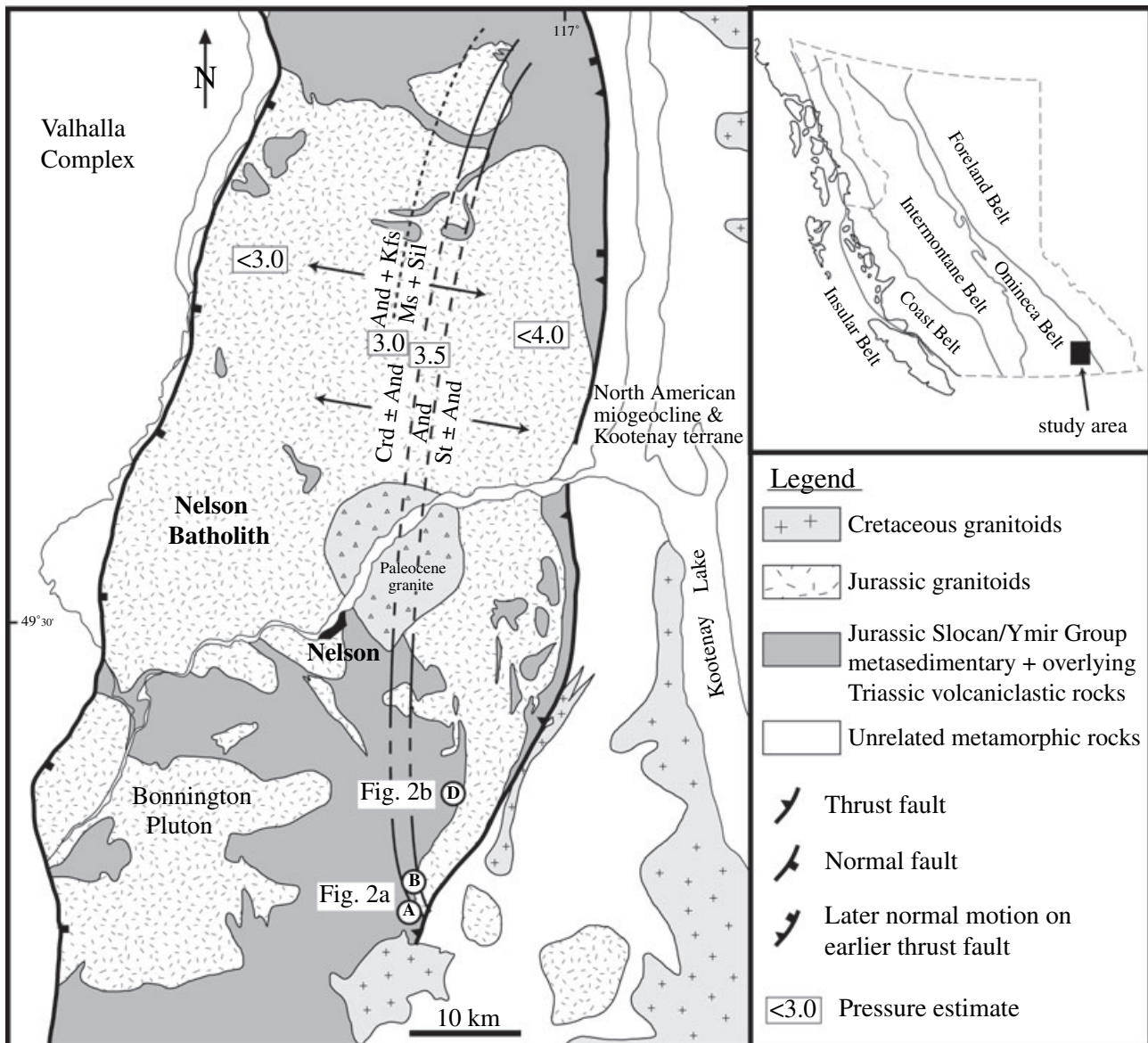
Fig. 1. Geology of the Nelson Batholith and surrounding contact metamorphosed rocks (from Pattison & Vogl, 2005). North–south trending bathograds result from post-metamorphic tilting of the aureole, exposing lower pressure, cordierite bearing schists in the west and south, and staurolite-bearing schists to the east. All three pressure domains are exposed sequentially in the tail from where samples for this study were collected (areas A, B and D, described in the text). Pressure estimates are from Pattison & Vogl (2005), based on mineral assemblages in pelitic rocks.

et al., 1988; Sweetkind & Duncan, 1989; Pattison & Vogl, 2005).

The contact aureole extends 0.7–2.0 km out from the Nelson Batholith into the surrounding metasediments (Pattison & Vogl, 2005) (see Figs 1 & 2). The isograds defining the aureole indicate that temperatures closest to the intrusion locally reached as high as ~700 °C (Pattison & Vogl, 2005). Post-intrusion tilting of the batholith and aureole resulted in contrasting prograde sequences of metamorphic minerals within rocks of similar composition (Pattison & Vogl, 2005). Metamorphic pressures range from ≥2.5 to ≤4.0 kbar,

which is reflected in the change from cordierite-bearing (lower pressure) to staurolite ± garnet-bearing rocks (higher pressure). This simple metamorphic setting therefore allows the behaviour of accessory phases to be examined in rocks of similar bulk composition and temperature range, but contrasting prograde mineral assemblage sequences.

Samples were collected along three transects perpendicular to contact metamorphic isograds (Fig. 2). From south to north, these correspond to transects A, B and D of Pattison & Vogl (2005). The three areas occur adjacent to each other along the southern tail of
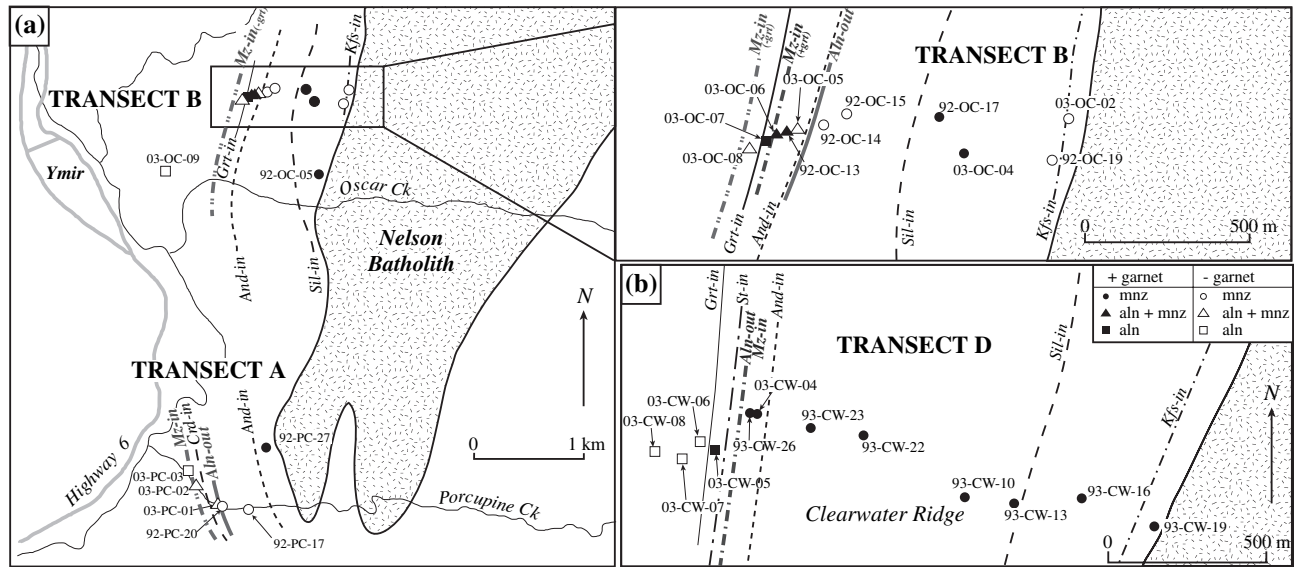
Fig. 2. Geology and sample location maps for (a) transects A (along Porcupine Creek) and B (near Oscar Creek), including an expanded view of transect B, and (b) transect D (along Clearwater Ridge). Modified from Pattison & Vogl (2005). Solid symbols indicate garnet-bearing samples, whilst open symbols indicate garnet-absent samples. The transects correspond to areas A, B and D indicated in Fig. 1. Rare earth element phase distribution is indicated by the symbols given in the key for (b). Xenotime is present in all samples, from all transects.

the Nelson Batholith, and are all hosted by graphitic metapelites of the Ymir Group. The southernmost (and lowest pressure) transect, transect A, contains the assemblage cordierite + biotite at intermediate grade, whereas the intermediate transect, transect B, is typified by the assemblage andalusite + biotite ± garnet at intermediate grade. The northernmost transect, transect D, is distinguished by staurolite + andalusite + biotite + garnet at intermediate grade. The pressure difference between transects A and D is ~1 kbar (Pattison & Vogl, 2005), as shown on Fig. 3.
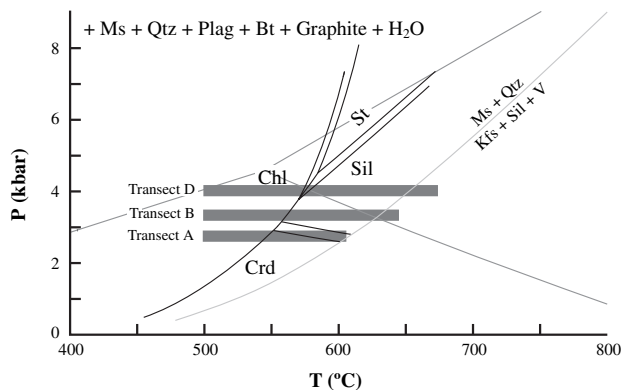

Fig. 3. Distribution of mineral assemblage sequences in P–T space for transects A, B and D. Modified from fig. 8 of Pattison & Vogl (2005). Mineral assemblage stabilities are calculated for the average Nelson metapelitic bulk composition using the thermodynamic data set of F.S. Spear, D.R.M. Pattison and J.T. Cheney (unpublished data, 2000; reported in Pattison *et al.*, 2002).

The effect of these differing mineral assemblages on the distribution of monazite and other Y + REE accessory phases is considered in detail below.

ANALYTICAL METHODS

Quantitative analyses (WDS) of monazite, xenotime, allanite, apatite and garnet and plagioclase were performed using the JEOL JXA-8200 electron microprobe at the University of Calgary, using both synthetic and natural standards and the ZAF correction method. Routine trace element analyses of monazite, xenotime, allanite and apatite were performed using an accelerating voltage of 20 kV and a probe current of 50 nA, with a 1 μm beam. Pulse-height analysis was used to set the baseline and window width to allow background level reduction and to minimize any high-order reflection peak interferences. Garnet was analysed for standard major elements plus Y, at 20 kV and 50 nA (1 μm beam). Plagioclase analyses were run at 10 kV and 10 nA.

In addition to WDS analyses, X-ray maps showing the distribution of Th and Y in monazite, Ce, P, Fe, and Ca in allanite-monazite breakdown textures, and Y and Ca in garnet were also collected by electron microprobe. For monazite and allanite-monazite textures, an accelerating voltage of 15 kV and current of 50 nA was used, with a 0.5–1.0 μm pixel size and 50 ms dwell time per pixel. Similarly, the garnet maps were run at 15 kV, 100 nA, 2 μm pixel size and 100 ms dwell time.

U-Pb and Th-Pb geochronological analyses were also performed using the JEOL JXA 8200 electron

microprobe, using the settings described in Yang & Pattison (2006). U, Th, Pb, La, Ce, Y and P were measured directly, whilst all other REEs were treated as Nd. Pb analysis was performed on two PET crystals simultaneously to essentially double the analysis time, thereby improving both precision and accuracy. An accelerating voltage of 15 kV, and 200 nA beam current were used, with a beam size ranging from 1 to 5 μm depending on grain size. Analyses were corrected for Th interference on the U Mβ peak using a correction factor of 0.006 determined from iterative correction on the ThO$_2$ standard with known UO$_2$ concentration. Any analyses returning PbO values lower than the detection limit of 200 p.p.m. were eliminated from the data set.

Bulk-rock XRF analyses were performed at McGill University, Montreal. Major element analyses were performed on fused beads prepared from ignited samples, whereas trace element analyses for the same samples were performed on pressed powder pellets. Detection limits for these data are based on three times the background sigma values.
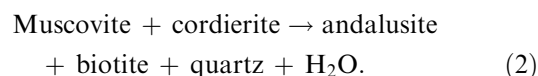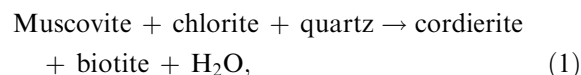
MAJOR PHASE PETROLOGY

A brief summary of the major mineral assemblages is given below, based on Pattison & Vogl (2005). Samples outside the contact aureole are the same in all three areas, consisting of muscovite-biotite-chlorite-plagioclase-quartz-ilmenite, with no garnet. These low-grade samples are all fine-grained, with the average grain size

< 100 μm. Whole-rock analyses from samples outside the aureole, and from each of the three transects, are given in Table 1.

Transect A

Figure 2a shows the isograds and distribution of samples along transect A. Upgrade of the regional grade argillites is a substantial cordierite zone, succeeded locally upgrade by the assemblage cordierite + andalusite, giving rise to cordierite-in and andalusite-in isograds. Rocks of this transect do not reach sillimanite grade. The reactions most likely responsible for these isograds are, respectively (Pattison & Vogl, 2005):

$$\text{Muscovite + chlorite + quartz} \rightarrow \text{cordierite} \\ \text{+ biotite + H}_2\text{O,} \qquad (1)$$

$$\text{Muscovite + cordierite} \rightarrow \text{andalusite} \\ \text{+ biotite + quartz + H}_2\text{O.} \qquad (2)$$

Bulk-rock chemistry of the transect A samples is shown in Table 1, as indicated by the sample prefix 'PC' (indicating 'Porcupine Creek').

Transect B

Transect B is characterized by a wide andalusite zone upgrade of the regionally metamorphosed meta-sedi-

Table 1. Bulk-rock data (major and trace elements) for representative samples from the Nelson contact aureole, transects A, B and D as described in the text. Major elements are in wt% oxide, whilst traces are in p.p.m.

Sample	Transect A				Transect B						Transect D			
	03-PC-03	03-PC-02A	03-PC-01B	92-PC-17A	03-OC-09A	03-OC-08	03-OC-06B	03-OC-05A	03-OC-04	03-OC-02B	03-CW-08B	03-CW-04A	93-CW-23	93-CW-19A
wt% oxide														
SiO$_2$	64.75	83.76	59.55	61.13	59.29	78.15	54.26	67.35	53.62	68.22	66.38	62.32	64.72	63.66
TiO$_2$	0.75	0.23	0.89	1.14	0.93	0.50	1.12	0.85	1.25	0.82	0.84	0.93	0.83	0.98
Al$_2$O$_3$	15.82	7.42	22.06	21.39	20.79	10.44	24.99	16.74	23.86	16.53	16.44	20.03	17.53	18.87
Fe$_2$O$_3$	5.44	2.25	4.98	4.52	4.22	2.91	5.10	5.24	6.95	5.64	5.55	6.42	6.29	5.83
MnO	0.07	0.02	0.18	0.10	0.03	0.03	0.18	0.09	0.49	0.09	0.06	0.09	0.08	0.21
MgO	3.38	0.54	2.03	1.51	2.03	0.83	1.71	1.97	2.02	2.04	2.51	1.71	1.74	2.28
CaO	3.34	0.65	0.77	0.38	1.05	0.78	0.24	0.42	1.49	0.57	1.53	0.66	0.74	0.59
Na$_2$O	1.00	0.85	0.69	0.81	0.41	0.85	0.80	0.53	1.76	0.69	0.77	0.61	0.76	0.70
K$_2$O	3.46	1.59	4.91	4.81	7.02	1.99	5.96	3.65	3.73	3.14	4.02	4.09	4.09	3.57
P$_2$O$_5$	0.19	0.10	0.13	0.14	0.16	0.19	0.10	0.16	0.13	0.12	0.15	0.15	0.18	0.13
LOI	1.32	2.22	3.58	3.93	4.28	2.93	5.29	3.29	4.93	2.24	1.92	3.32	3.69	2.44
Total	99.61	99.67	99.83	99.96	100.29	99.66	99.83	100.36	100.35	100.16	100.23	100.40	100.20	100.17
X_{Mn}[a]	0.01	0.01	0.03	0.02	0.01	0.01	0.03	0.02	0.07	0.02	0.01	0.01	0.01	0.04
X_{Ca}[b]	0.77	0.43	0.53	0.32	0.72	0.48	0.23	0.44	0.46	0.45	0.67	0.52	0.49	0.46
Y	30	19	35	42	34	34	40	32	39	32	31	29	34	34
Ce	92	<d/l	63	14	99	60	83	140	130	78	89	96	98	114
Nb	3	14	10	<d/l	8	19	10	9	13	7	6	9	6	7
Pb	10	6	18	11	4	11	16	13	42	20	15	13	15	22
Th	16	<d/l	19	23	20	3	22	16	21	15	17	19	17	16
U	<d/l	5	<d/l	<d/l	<d/l	5	<d/l	<d/l	<d/l	<d/l	<d/l	<d/l	<d/l	<d/l
Rb	126	50	186	177	237	72	223	137	157	123	137	126	127	170
Sr	362	139	201	174	119	197	199	138	386	196	134	188	269	239
Zr	219	90	170	422	210	143	253	213	306	225	251	209	211	247

$<$d/l = below detection limit.
[a]X_{Mn} = Mn/(Mn + Fe).
[b]X_{Ca} = Ca/(Ca + Na).

ments. This zone is succeeded upgrade by a sillimanite zone and, at the highest grade, a sillimanite + K-feldspar zone (Fig. 2a). Downgrade of the andalusite-in isograd, garnet is locally developed in Mn-rich layers, giving rise to a narrow garnet zone and garnet isograd not shown in Pattison & Vogl (2005). This garnet was termed 'Early Garnet' or Grt(e) by Pattison & Vogl (2005), owing to its development prior to any other porphyroblast phases. The location of the transect B garnet-in isograd may not represent a true reaction isograd, but rather the lowest grade occurrence of appropriately composed bulk rock.

Garnet(e) is interpreted to have formed by the reaction:

$$Muscovite + chlorite + quartz \rightarrow garnet + biotite + H_2O. \quad (3)$$
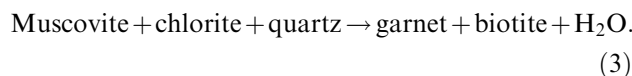
Andalusite formation is attributed to the reaction:

$$Muscovite + chlorite + quartz \rightarrow andalusite + biotite + H_2O, \quad (4)$$

whilst sillimanite formation is ascribed to:

$$Andalusite \rightarrow sillimanite. \quad (5)$$

Andalusite is generally still present as relic grains in the sillimanite zone that are increasingly replaced by sillimanite as grade increases. The development of K-feldspar is due to the reaction:

$$Muscovite + quartz \rightarrow Al_2SiO_5 + K\text{-}feldspar + liquid. \quad (6)$$

Samples from transect B are indicated in Table 1 by the prefix 'OC' (for 'Oscar Creek').

Transect D

Figure 2b shows the distribution of isograds and samples for transect D. The main metamorphic zones are, with increasing grade: staurolite, andalusite, sillimanite and K-feldspar. A garnet-in isograd is shown in Fig. 2b that was not described by Pattison & Vogl (2005), and is based on the local development of Garnet(e) in argillites immediately (<50 m) downgrade of the staurolite zone. The Grt(e)-in reaction for transect D is considered to be the same as reaction (3) described for transect B, above. In terms of bulk composition, the transect D samples, all of which contain garnet, do not show the same variation in Mn content as seen in transect B (Table 1). The bulk composition of most samples from transect D is similar to that of transect A samples and the garnet-absent transect B samples.

The staurolite-in, andalusite-in, sillimanite-in and K-feldspar-in isograd reactions are interpreted as follows (Pattison & Vogl, 2005):
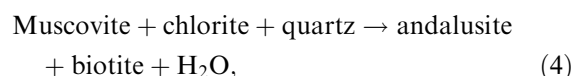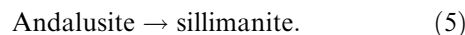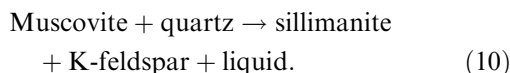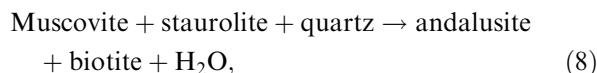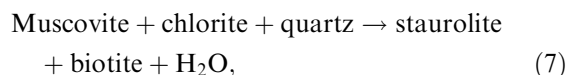
Fig. 4. BSE images from each transect demonstrating the reaction sequence from an allanite-dominant assemblage at low grades (left) to monazite-dominant at high grade (right). Note that sample 93-CW-13 in the lower grade position relative to sample 93-CW-26 (the reverse of which is shown in Fig. 2b) to demonstrate the reactant/product relationship between allanite and monazite prior to inclusion in staurolite. (a), (e), (i) and (m): Typical euhedral precursor allanite in a muscovite-biotite-quartz ± chlorite matrix from each transect. These samples contain no monazite. The allanite in (m) coexists with garnet. (b) Fine-grained, anhedral monazite around allanite (outlined with dashed line) from transect A, below the cordierite-in isograd, with associated remnant allanite amongst the monazite grains (transect A). (c) Monazite cluster included in cordierite, with associated remnant allanite amongst the monazite grains (transect A). (d) Monazite cluster showing pseudomorphous shape after allanite, in muscovite-biotite-quartz matrix with retrograde chlorite (transect A). (f) Monazite corona around allanite (garnet-absent transect B). The bright corona also contains a fine-grained Fe-rich phase, possibly magnetite, with apatite and plagioclase abundant in the matrix. (g) Monazite consuming allanite in the precursor to a cluster, no longer with the coronal morphology (garnet-absent transect B). (h) Coarse-grained cluster monazite at highest grade in the transect B (sill + kfs bearing, garnet-absent). Some of these grains show minor grain boundary resorption possibly because of grain dissolution from the presence of small amounts of melt. Note the difference in magnification between images in this series. (i) Allanite coexisting with garnet (garnet-bearing transect B). The allanite shows signs of instability and grain dissolution, however its original euhedral shape is still recognizable. Monazite is rare in this sample. (k) Incipient monazite adjacent to ragged allanite (garnet-bearing transect B). In this high-grade sample the monazite (sillimanite-grade, garnet-bearing transect B). (l) Lone monazite in biotite-quartz-plagioclase matrix (sillimanite-grade, garnet-bearing transect B). (n) Primary allanite and monazite inclusions in staurolite (transect D). (o) Small, anhedral, low-grade lone monazite has undergone coarsening and smoothing of the grain boundaries. (p) Typical lone monazite in qtz-bt matrix (andalusite grade, transect D). Abbreviations: aln = allanite, mz = monazite, st = staurolite, bt = biotite, qtz = quartz, ilm = ilmenite.

Muscovite + chlorite + quartz → staurolite
+ biotite + H_2O,   (7)

Muscovite + staurolite + quartz → andalusite
+ biotite + H_2O,   (8)

Andalusite → sillimanite,   (9)

Muscovite + quartz → sillimanite
+ K-feldspar + liquid.   (10)

Most garnet in transect D, up to and including that in the andalusite zone, is interpreted to be Grt(e), based on its occurrence as inclusions in all other porphyroblasts and its euhedral, largely un-resorbed texture (Pattison & Vogl, 2005). Within the sillimanite zone, a later generation of garnet, Grt(l), appears locally, the origin of which is unclear.

Samples from transect D are indicated in Table 1 by the prefix 'CW' (for 'Clearwater Creek').

ACCESSORY MINERAL DISTRIBUTION AND TEXTURES

Samples of the regional protolith from each transect were collected and examined petrologically to establish the character, composition and distribution of REE-bearing accessory phases outside of the aureole. These samples represent the starting assemblages prior to contact metamorphism. In all samples, regardless of transect, the dominant REE accessory phase in rocks unaffected by contact metamorphism is allanite. Of the phosphates, monazite is absent, apatite is ubiquitous, and xenotime is common.

Allanite occurs as sub- to euhedral grains, generally up to 170 μm long and 30 μm wide (Fig. 4a). It is commonly poikiloblastic, with inclusions of quartz. Allanite is interpreted to be metamorphic, rather than detrital or an alteration phase, and to have formed in association with the older, regional, low-grade metamorphism. Wing *et al.* (2003) described similar euhedral allanite grains in biotite-grade regionally metamorphosed rocks, like those in the Nelson area, and inferred that the allanite replaced pre-existing monazite. We see no evidence of a precursor to euhedral allanite here. Table 2 lists allanite analyses from three low-grade samples.

Apatite occurs in all samples outside the contact aureole, and is sub- to anhedral, with a grain size typically ~25–30 μm. Based on its fragmented and anhedral texture, apatite is interpreted to be of detrital rather than metamorphic origin. In transect A, regional-grade apatite is commonly strongly zoned with respect to Y and the LREEs Ce and Nd, with these elements enriched in the core and depleted towards the rims.

Xenotime is generally anhedral, and commonly associated with detrital zircon. Diagenetic xenotime is a common phase in low-grade shales and slates and

Table 2. Allanite rim analyses for low-grade samples, outside the contact aureole. All analyses are in wt% oxide.

Sample No.	Transect A 03-PC-03	Transect B 03-OC-09A	Transect D 03-CW-08B
SiO_2	33.68	35.49	33.04
TiO_2	0.08	0.08	0.49
Al_2O_3	20.72	20.46	21.02
FeO	11.22	10.51	11.46
MnO	0.13	< d/l	0.19
MgO	0.35	0.33	0.26
CaO	12.13	12.05	12.45
Na_2O	< d/l	< d/l	< d/l
K_2O	0.21	0.05	0.09
P_2O_5	0.03	0.11	0.11
Y_2O_3	0.33	0.21	0.38
La_2O_3	4.61	4.17	4.59
Ce_2O_3	10.02	9.92	9.90
Pr_2O_3	0.84	0.70	0.77
Nd_2O_3	4.20	3.83	3.84
Sm_2O_3	0.59	0.70	0.43
Eu_2O_3	0.17	0.17	0.13
Gd_2O_3	0.35	0.31	0.35
Dy_2O_3	0.03	0.05	0.13
Er_2O_3	0.04	0.02	0.03
Yb_2O_3	< d/l	0.01	< d/l
Lu_2O_3	0.03	0.03	0.06
ThO_2	0.61	0.87	0.66
UO_2	0.07	< d/l	< d/l
Total	100.44	100.07	100.38

other sediments worldwide (Rasmussen, 1996) and has been found to overgrow detrital zircon (with which it is isostructural) during the early stages of diagenesis (e.g. Rasmussen *et al.*, 1998; Fletcher *et al.*, 2000).

Transect A

The lowest grade occurrence of monazite in transect A is in sample 03-PC-02, upgrade of primary allanite-bearing sample 03-PC-03 (Fig. 4b). Monazite occurs as numerous grains partially surrounding anhedral allanite (Fig. 4b). Away from allanite, monazite is rare or absent.

Further upgrade towards the batholith in the cordierite zone (sample 03-PC-01B), monazite occurs as elongate clusters with only minor associated allanite (Fig. 4c). The monazite cluster in Fig. 4c is included in a cordierite porphyroblast, and the allanite is restricted to the area between monazite grains. No allanite is found elsewhere in the matrix. At higher grade still (sample 92-PC-17a), the dominant form of monazite is that of discrete clusters with no remaining allanite (Fig. 4d). In the example shown in Fig. 4d, monazite clusters are observed intergrown with chlorite. Given that primary chlorite disappeared in the cordierite zone (Pattison & Vogl, 2005), and that sample 92-PC-17a contains abundant cordierite, the chlorite observed intergrown with monazite in 92-PC-17a is likely to be of secondary origin. Similar clusters of monazite are found throughout the area, and only in one sample was the textural relationship with chlorite observed. Monazite in sample 92-PC-17A is therefore unlikely to be itself secondary, rather that secondary chlorite has formed near pre-existing monazite. From low to high grade, transect A
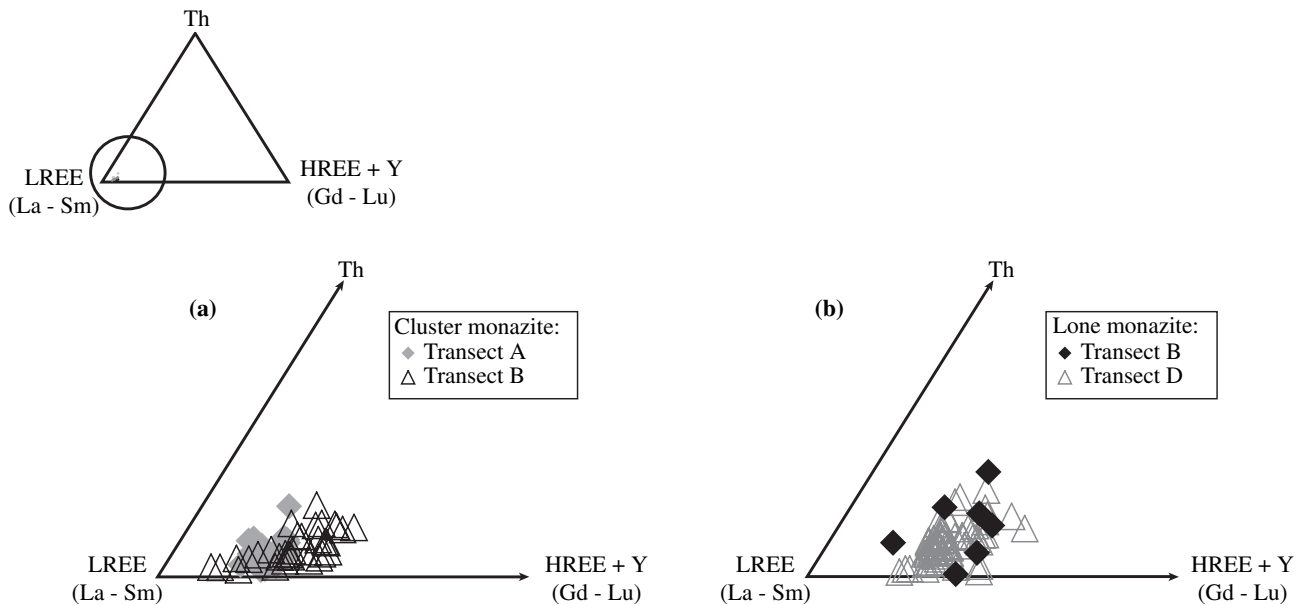
Fig. 5. Ternary Th-LREE-HREE + Y diagrams for Nelson aureole monazite. The LREE corner of the ternary has been enlarged to more clearly depict variation in the populations. (a) Cluster monazite from transects A and B (garnet-absent), (b) lone monazite from transect B (garnet-bearing) and transect D.

cluster monazite is uniform in composition, as demonstrated on the LREE-HREE + Y-Th ternary shown in Fig. 5a.

Xenotime occurs in all samples from transect A, but does not appear to have any consistent spatial or textural relationship to the monazite clusters. In rare cases, xenotime does occur near or next to monazite. These grains show no sign of physical reaction, and have the same composition as monazite and xenotime elsewhere in the sample. With increasing grade, xenotime becomes coarser grained, up to 40 μm in 92-PC-17a and 92-PC-27 relative to 5–10 μm in samples 92-PC-20 and 03-PC-01B.

Transect B

As outlined above, some transect B samples contain garnet, and some do not, depending on the Mn content of the rocks. As the monazite response in garnet-bearing *v.* garnet-absent samples differs quite markedly, they will be described separately.

Garnet-absent samples

The lowest grade occurrence of monazite in the garnet-absent transect is in sample 03-OC-08. In this sample, coronas of monazite occur around coarse, anhedral allanite (Fig. 4f). Upgrade, the cluster morphology described in transect A is again observed (Fig. 4g), with monazite as the dominant LREE phase, and no primary allanite anywhere in the assemblage. The cluster monazite is unzoned and varies little in composition with grade (Table 3 & Fig. 5). The only change going

upgrade is a coarsening of grain size and lessening of the number of grains in each cluster (Fig. 4h).

With increasing grade, apatite becomes more rounded and coarser grained, although any increase or decrease in modal abundance could not be ascertained. Xenotime is present even to the highest grades within the aureole (e.g. sample 92-OC-19B). It is commonly associated with zircon, a relationship that has likely persisted from diagenesis (e.g. Rasmussen, 1996; Rasmussen *et al.*, 1998). The modal abundance of xenotime does not appear to change measurably with increasing grade. Some coarsening of xenotime grain size, from < 10 μm to ≥10 μm, is apparent, accompanied by a smoothing of the grain shape.

Garnet-bearing samples

The distribution of garnet-bearing samples for transect B is shown on Fig. 2a. The first occurrence of garnet (sample 03-OC-07) is at slightly higher grade than the first occurrence of monazite in the garnet-*absent* samples described above (sample 03-OC-08). Initially garnet and allanite are found to coexist with no monazite in the assemblage (Fig. 4j). Upgrade, in sample 92-OC-13, rare monazite is found along allanite grain boundaries. The textural relationship developed in this case bears only a tenuous resemblance to the clear coronal or pseudomorphous clusters of monazite described for the garnet-absent transect. Allanite in samples 03-OC-07 and 92-OC-13, both near the andalusite-in isograd, is more anhedral than the pre-contact metamorphic allanite, however the original primary morphology is still evident in most cases (Fig. 4j).

Table 3a. Representative monazite analyses used for thermometric calculations given in Table 4.

wt% oxides	92-PC-20	92-PC-17	92-PC-27	92-OC-14	92-OC-15	92-OC-19	92-OC-13	03-OC-06B	92-OC-17	03-OC-04	92-OC-05B	03-CW-04	93-CW-23	93-CW-10	93-CW-16
SiO_2	1.30	0.79	0.25	0.78	0.19	0.12	3.22	0.79	0.16	0.07	0.19	0.08	0.04	<d/l	0.03
CaO	0.59	1.11	0.49	0.50	0.88	1.05	0.92	0.92	0.38	1.33	1.12	0.83	0.86	0.88	0.77
P_2O_5	30.13	29.44	30.06	29.39	29.72	30.51	28.11	29.50	29.57	29.71	30.50	29.42	28.96	30.87	29.67
Y_2O_3	1.34	1.18	1.44	1.85	1.64	2.25	0.93	1.29	1.90	1.51	2.52	1.39	1.42	1.83	2.08
La_2O_3	13.80	12.46	14.71	14.35	13.01	14.46	14.45	15.63	13.29	12.22	13.10	13.30	13.64	14.60	14.60
Ce_2O_3	28.83	26.62	28.24	27.18	27.32	25.39	27.29	27.84	29.26	26.30	25.97	25.82	27.36	27.63	27.84
Pr_2O_3	2.99	2.99	3.04	2.70	3.08	3.00	2.79	3.02	3.37	2.86	2.96	2.69	3.12	3.06	2.79
Nd_2O_3	12.60	12.21	12.75	12.29	12.62	11.93	11.87	11.99	14.34	11.99	11.86	11.65	13.04	11.98	12.71
Sm_2O_3	1.79	1.88	1.94	1.74	1.84	1.49	1.42	1.54	1.89	1.58	1.71	1.64	1.84	1.53	1.66
Eu_2O_3	0.17	0.19	0.27	<d/l	0.22	<d/l	0.03	0.16	0.08	0.09	<d/l	0.13	0.06	0.20	0.14
Gd_2O_3	1.14	1.21	1.77	1.29	1.59	1.38	0.94	1.00	1.47	1.68	1.73	1.61	1.93	1.26	1.36
Dy_2O_3	0.49	0.50	0.67	0.61	0.42	0.50	0.36	0.49	0.67	0.72	0.73	0.56	0.61	0.59	0.79
Er_2O_3	0.11	0.06	0.09	<d/l	0.13	<d/l	<d/l	<d/l	<d/l	<d/l	<d/l	<d/l	<d/l	<d/l	<d/l
Yb_2O_3	<d/l	<d/l	<d/l	<d/l	<d/l	<d/l	<d/l	<d/l	<d/l	<d/l	<d/l	<d/l	<d/l	<d/l	<d/l
Lu_2O_3	0.11	0.13	0.14	0.07	0.14	0.06	0.10	0.09	0.17	0.15	<d/l	0.16	0.17	0.15	0.18
ThO_2	2.33	6.33	1.85	1.75	3.85	4.94	3.27	3.46	0.86	6.15	4.84	3.82	4.75	0.84	3.11
UO_2	<d/l	<d/l	<d/l	0.38	0.33	0.55	0.31	0.37	<d/l	0.55	0.69	0.05	0.33	0.11	<d/l
Total	97.72	97.10	97.71	94.88	96.98	97.63	96.01	98.09	96.47	97.98	97.04	92.95	97.79	94.57	97.73
$X(Y+HREE)PO_4$	0.05	0.05	0.06	0.06	0.06	0.06	0.02	0.03	0.07	0.03	0.06	0.06	0.06	0.07	0.07

Table 3b. Garnet analyses used for monazite thermometry.

wt% oxides	92-OC-13		03-OC-06B		92-OC-17		03-OC-04		92-OC-05B		03-CW-04		93-CW-23		93-CW-10		93-CW-16	
	Core	Rim	Core	Rim	Core	Rim	Core	Rim	Core	Rim	Core	Rim	Core	Rim	Core	Rim	Core	Rim
SiO_2	36.80	36.87	36.36	35.61	37.32	37.48	35.72	36.03	36.8	37.07	36.64	36.6	36.44	36.61	36.39	36.08	36.94	36.71
TiO_2	0.05	0.03	0.06	0.04	<d/l	<d/l	0.03	0.03	<d/l	<d/l	0.03	0.02	0.06	0.01	0.01	0.02	0.01	0.02
Al_2O_3	20.94	21.17	21.93	22.83	20.51	20.44	21.95	22.19	20.2	20.55	20.96	20.87	21.34	21.07	22.52	22.43	20.86	20.86
Cr_2O_3	<d/l	0.06	0.01	0.04	<d/l	<d/l	0.01	0.01	<d/l	0.01	0.01	0.01	0.01	<d/l	0.01	0.01	0.02	0.05
FeO	24.47	25.33	23.36	24.72	26.67	28.33	28.68	28.81	28.75	28.49	33.73	34.67	30.46	31.75	33.00	33.29	29.17	29.70
MnO	14.48	13.30	15.88	13.98	12.31	10.39	9.56	9.91	9.05	9.30	4.55	3.87	6.99	6.01	4.22	4.36	9.83	10.66
MgO	1.45	1.42	1.51	1.85	2.45	2.37	2.71	2.57	2.60	2.48	2.15	2.10	2.32	2.19	2.84	2.74	2.61	1.88
CaO	1.11	1.31	1.39	1.24	0.95	1.23	1.08	0.71	1.03	1.27	1.21	1.08	2.04	1.69	1.71	1.46	2.05	1.85
Y_2O_3	0.18	0.21	0.24	0.18	0.08	0.04	0.09	0.05	0.04	0.03	0.21	0.12	0.24	0.05	0.24	0.06	0.27	0.05
Total	99.48	99.64	100.74	100.46	100.29	100.28	99.85	100.30	98.48	99.20	99.48	99.34	99.91	99.39	100.94	100.45	101.74	101.76
X_{Ca}	0.03	0.04	0.04	0.04	0.03	0.04	0.03	0.02	0.03	0.04	0.04	0.03	0.06	0.05	0.05	0.04	0.06	0.05
X_{YAG}	0.0027	0.0032	0.0035	0.0026	0.0012	0.0006	0.0013	0.0007	0.0006	0.0005	0.0031	0.0017	0.0034	0.0008	0.0034	0.0009	0.0037	0.0007
Y (p.p.m.)	1441	1685	1906	1394	661	346	740	409	331	260	1669	913	1850	417	1874	472	2126	378

Table 3c. Apatite analyses used for monazite thermometry.

wt% oxides	92-OC-13	03-OC-06B	92-OC-17	03-OC-04	92-OC-05B	03-CW-04	93-CW-23	93-CW-10	93-CW-16
SiO_2	0.19	0.24	0.06	0.03	0.04	0.26	0.15	0.07	0.09
FeO	0.14	0.32	0.06	0.17	0.15	0.16	0.25	0.44	0.45
MnO	0.15	0.15	0.13	0.15	0.24	0.06	0.08	0.17	0.14
MgO	<d/l	0.01	<d/l	0.01	0.01	<d/l	0.01	0.03	<d/l
CaO	55.61	54.91	55.54	55.64	54.30	53.90	54.76	56.74	57.80
Na_2O	0.04	0.08	0.03	0.03	0.04	0.02	0.05	0.04	0.05
P_2O_5	40.80	40.30	40.80	40.42	40.61	35.49	41.31	39.32	40.59
SrO	0.01	0.03	<d/l	0.03	0.03	0.04	0.02	0.03	0.03
Y_2O_3	0.18	0.15	0.07	0.07	0.12	0.05	0.07	0.10	0.06
La_2O_3	<d/l	<d/l	<d/l	<d/l	<d/l	<d/l	<d/l	<d/l	<d/l
Ce_2O_3	0.05	0.08	0.03	0.03	0.04	0.01	0.04	0.03	0.02
Nd_2O_3	0.04	0.06	0.03	0.01	0.02	<d/l	0.02	0.01	<d/l
ThO_2	0.01	0.03	<d/l	0.01	0.03	<d/l	<d/l	<d/l	<d/l
F	3.37	3.99	3.29	3.37	4.07	3.29	4.02	3.85	2.61
Cl	0.04	0.03	0.06	0.08	0.09	0.02	0.02	0.03	0.01
Total	100.64	100.38	100.08	100.03	99.78	93.31	100.79	100.84	101.85
X_{OH}	0.33	0.41	0.46	0.46	0.50	0.84	0.32	0.30	0

In garnet-bearing samples upgrade of 03-OC-07, monazite takes a different form to that seen in the garnet-absent samples of transects B and A, occurring as lone grains in the sample matrix with no obvious clustering of grains. There is an overall coarsening of grain size, and rounding of grain shape to a more equi-

Table 3d. Plagioclase analyses used for monazite thermometry.

wt% oxides	92-OC-13	03-OC-06B	92-OC-17	03-OC-04	92-OC-05B	03-CW-04	93-CW-23	93-CW-10	93-CW-16
SiO_2	63.00	67.66	62.11	63.85	63.06	63.81	61.03	61.29	59.04
Al_2O_3	22.39	20.32	24.39	22.86	22.61	22.95	25.81	25.48	26.33
CaO	3.44	0.43	4.96	3.14	3.93	0.11	6.32	5.98	6.96
Na_2O	9.15	11.12	8.51	9.40	8.47	3.91	7.84	7.90	7.57
K_2O	0.34	0.14	0.06	0.20	0.14	9.07	0.16	0.12	0.18
P_2O_5	< d/l	0.01	0.17	0.26	0.13	0.08	0.04	0	0.05
Total	98.33	99.68	100.20	99.70	98.33	99.93	101.20	100.77	100.13
X_{Ca}	0.17	0.02	0.24	0.16	0.20	0.19	0.44	0.30	0.34

dimensional form (as opposed to the anhedral, poikilitic form of the more incipient monazite found at low grade). Monazite is only rarely found included in garnet, with the majority occurring in the matrix amongst plagioclase and quartz, and in some instances, biotite.

The lone monazite in the garnet-bearing samples is compositionally more heterogeneous than the cluster monazite from garnet-absent samples (Fig. 5). The lowest grade lone monazite (garnet zone) commonly has a diffuse Th-enriched core (Fig. 6a), which is interpreted to represent Th fractionation, analogous to Mn-rich cores in garnet (e.g. Kohn & Malloy, 2004). The diffuse, high-Th core may, although not in every case, persist into the andalusite-zone, as seen in Fig. 6a. In the sillimanite and sillimanite + K-feldspar zones, most monazite is unzoned. However, where compositional zonation is present, there is consistent Th and Y enrichment towards the rims, outwards from a Th + Y-depleted core (e.g. Fig. 6c,d). In these high-grade examples, there is no evidence of an original Th-enriched core.

Xenotime is present in every sample from low to high grades, and is generally rounded with a typical grain size of up to c. 20 μm. Some grain coarsening is evident with increasing grade, and xenotime is also commonly included in garnet, whilst also occurring as a matrix phase (e.g. sample 03-OC-04). Where xenotime occurs in the matrix near garnet, no embayment or dissolution of the garnet is apparent. Apatite distribution and abundance in the transect B garnet-bearing samples is similar to that described for the garnet-absent samples. It is a ubiquitous phase, coarsening with increasing grade.
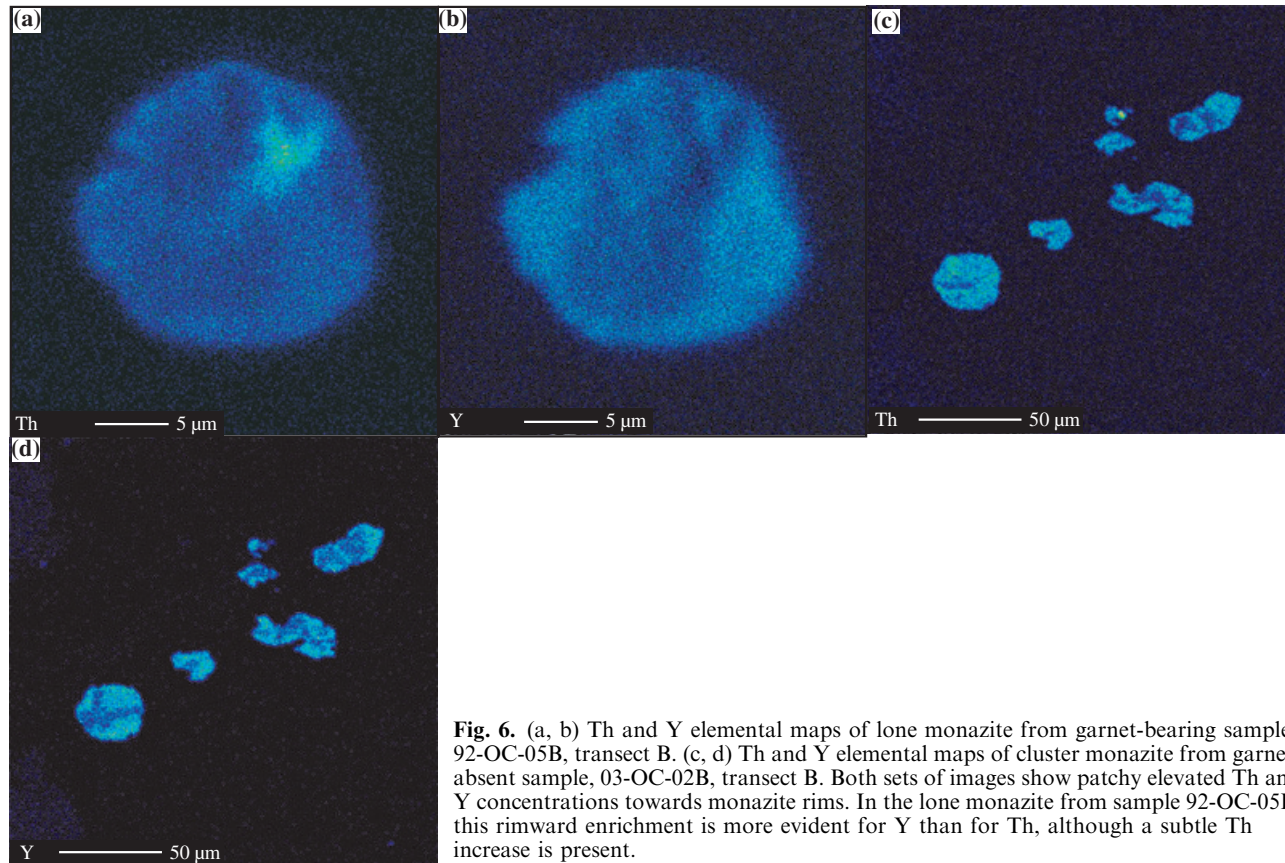

Fig. 6. (a, b) Th and Y elemental maps of lone monazite from garnet-bearing sample, 92-OC-05B, transect B. (c, d) Th and Y elemental maps of cluster monazite from garnet-absent sample, 03-OC-02B, transect B. Both sets of images show patchy elevated Th and Y concentrations towards monazite rims. In the lone monazite from sample 92-OC-05B, this rimward enrichment is more evident for Y than for Th, although a subtle Th increase is present.

Transect D

As in the garnet-bearing samples from transect B, allanite without monazite is present in samples from the lowest grade part of the garnet zone in transect D. In sample 03-CW-05A (Fig. 2b), euhedral allanite coexists with small, euhedral grains of garnet(e) (Fig. 4m). The allanite in this case is less corroded than allanite from garnet zone samples 92-OC-13 and 03-OC-07 in transect B that contain the same mineral assemblage. Allanite co-existing with garnet in transect D has the same morphology, grain size, matrix distribution and composition as that in the sub-garnet grade samples of this and other transects (e.g. that shown in Fig. 4a, compositions given in Table 2). In the staurolite zone, ∼15 m further upgrade within the contact aureole, allanite is absent from the matrix assemblage, and the dominant LREE phase is monazite. Figure 4n shows monazite and allanite preserved together as inclusions within staurolite.

The lowest grade occurrence of monazite is in staurolite-bearing samples 93-CW-26 and 03-CW-04 (Fig. 2b). It is fine-grained, largely anhedral (Fig. 4o) and occurs as isolated, individual grains, mainly in the matrix. Cluster morphologies are rare, and in these cases it is unclear as to whether or not the clusters are a coincidental grouping of monazite grains or a pseudomorphous clustering similar to that described for transects A and B. Once formed, monazite becomes coarser grained with increasing grade, and shows more regular, rounded, grain boundaries. In these samples, allanite is absent.

Compositional zonation, especially with respect to Th and Y, follows the same trend as the transect B garnet-bearing monazite (see Fig. 6). Downgrade of the sillimanite zone, monazite is unzoned. At or above sillimanite grade, monazite shows an increase in Th and Y towards the rims.

Of the other REE phosphates, apatite is again ubiquitous as described for transects A and B. Xenotime is present in all samples from low to high grade. Above the staurolite isograd, xenotime is found both as inclusions in garnet as well as in the sample matrix. Some HREE zonation in xenotime is also present, especially at and above sillimanite-grade.

Mechanisms of monazite formation

Garnet-absent rocks

The distribution of accessory phase isograds (Fig. 2), coronal monazite textures around allanite and cluster monazite morphologies at higher grade all indicate that monazite forms from the breakdown of allanite in garnet-absent assemblages of the Nelson aureole. In transect A, the pseudomorphous clusters of monazite are clearly developed, with remnant allanite preserved amongst monazite included in cordierite (Fig. 4c). As monazite clusters elsewhere in the sample do not have any allanite associated with them, this texture is interpreted to indicate that the monazite-forming reaction was unable to go to completion, perhaps because allanite was separated from other reactant phases (e.g. apatite?) due to envelopment by cordierite. The monazite clusters observed in transect A are reminiscent of those described by Wing *et al.* (2003) and Fraser *et al.* (2004), the latter which occur in similar garnet-absent, cordierite-bearing rocks.

In transect A, the cordierite-in isograd represents significant reaction of chlorite + muscovite to form cordierite + biotite. Despite the major change in silicate assemblage and dehydration of the rocks, this reaction does not appear to affect accessory mineral distribution or texture at all. It is worth noting that the boundary of the contact aureole as defined by silicate assemblages is at the cordierite-in isograd. The lowest grade occurrence of monazite in transect A is ∼100 m further downgrade, and as such the accessory mineral reactions in this case have extended the detectable limits of contact metamorphism.

The development of monazite coronae around allanite is most clearly seen in the garnet-absent samples of transect B (e.g. sample 03-OC-08). Figure 7 shows Ca, Ce, Fe and P maps of the texture from Fig. 4f, allowing the participant minerals in the reaction to be clearly identified. The Ca map (Fig. 7a) shows the distribution of apatite, whereas the Ce map (Fig. 7b) shows the concentration of monazite (Ce + P highs) around the outside of the allanite porphyroblast. The Fe map (Fig. 7c) shows the incorporation of an Fe-rich phase (only Fe and Si peaks identifiable on EDS scan) in the monazite corona around allanite, which most likely is magnetite intergrown with quartz. This suggests that an Fe-oxide is a by-product of Fe-bearing allanite breakdown. Plagioclase is abundant throughout the sample matrix, and occurs within close textural proximity to the reaction textures. It is invoked as a product phase for reaction (11), below, to incorporate Al and Si released from allanite, and Ca from apatite.

The qualitative reaction written for monazite formation in transects A and B (garnet-absent) on the basis of textural relationships is:

$$\text{Allanite} + \text{apatite} \rightarrow \text{monazite}$$
$$+ \text{plagioclase} + \text{magnetite(?)}. \qquad (11)$$
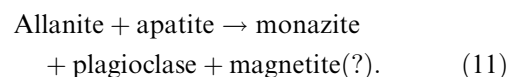
Xenotime is found in all samples examined for this study, but is not included as either a reactant or a product phase in reaction (11). It may rarely occur adjacent to/in contact with monazite, but for the most part it shows no textural relationship with monazite or allanite. Xenotime does increase in grain size with increasing grade within the aureole. Whereas the abundance of monazite increases markedly with the breakdown of allanite, the abundance of xenotime does not appear to change at all in response to allanite breakdown and monazite growth. These observations
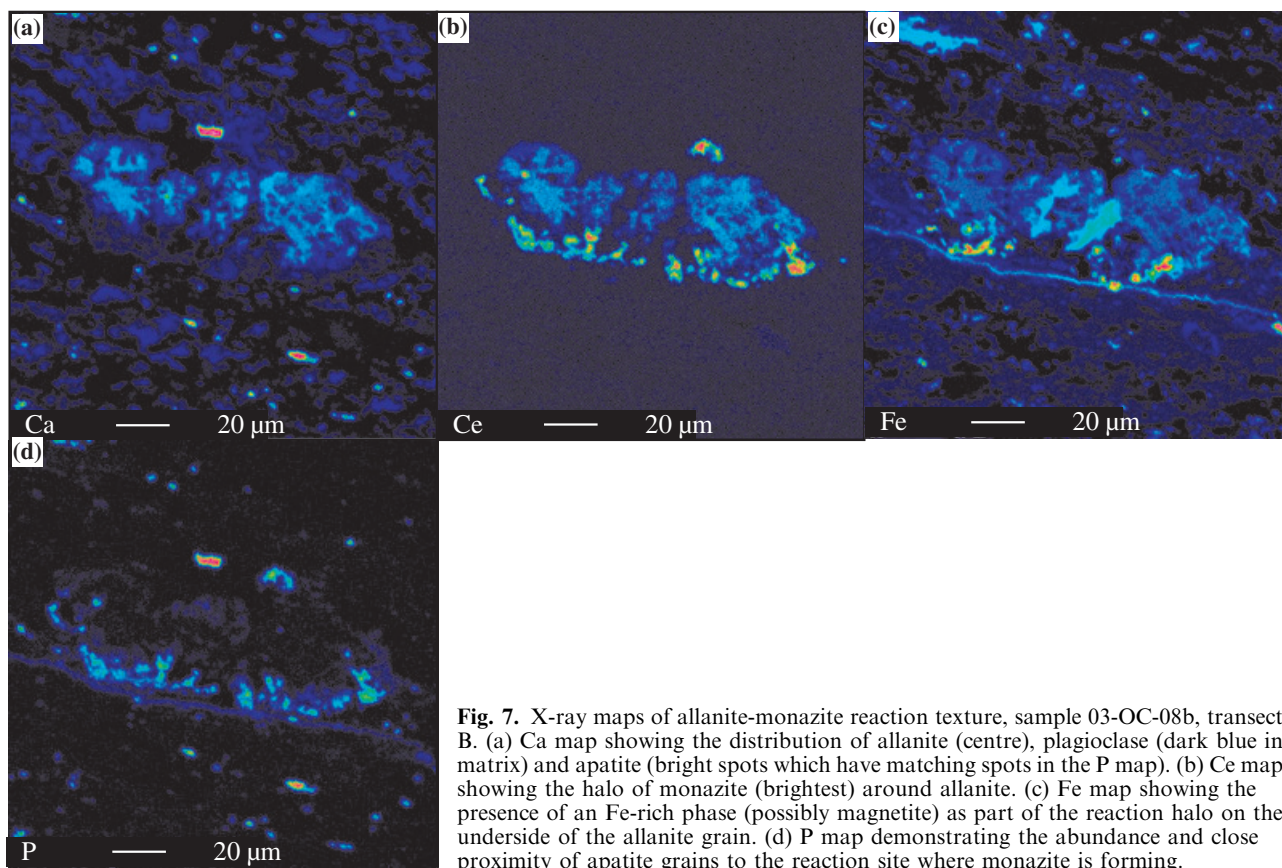
Fig. 7. X-ray maps of allanite-monazite reaction texture, sample 03-OC-08b, transect B. (a) Ca map showing the distribution of allanite (centre), plagioclase (dark blue in matrix) and apatite (bright spots which have matching spots in the P map). (b) Ce map showing the halo of monazite (brightest) around allanite. (c) Fe map showing the presence of an Fe-rich phase (possibly magnetite) as part of the reaction halo on the underside of the allanite grain. (d) P map demonstrating the abundance and close proximity of apatite grains to the reaction site where monazite is forming.

suggest that whilst xenotime coexists with monazite, it is not modally involved in monazite formation.

Garnet-bearing rocks

In contrast to the clearly pseudomorphous textures of transects A and garnet-absent B, the textural features of monazite in the garnet-bearing samples of transects B and D are less easily interpreted. However the formation of monazite in the garnet-bearing samples of transect B still appears to be related to the breakdown of allanite (Fig. 4k). Allanite, despite being common in the pre-contact assemblage, as well as coexisting with garnet in samples 03-OC-07 and 03-CW-05, is absent from the rocks containing both garnet and monazite. Evidence that it was once present is confirmed by the occurrence of allanite inclusions in garnet (sample 92-OC-05b). This allanite has a similar composition to the pre-contact, euhedral allanite (see Table 2).

In transect D, no pseudomorphous reaction textures of monazite after allanite have been observed. However, monazite and allanite have been found rarely as intimately related inclusions occurring together within minerals such as garnet and staurolite near the silli-manite-in isograd (Fig. 4n). In samples where such inclusion relationships exist, allanite is absent from the matrix assemblage.

Comparison between garnet-bearing and garnet-absent absent rocks

The main differences between the garnet-absent and garnet-bearing transects relate to the spatial distribution of allanite and monazite with respect to the silicate reactions/isograds, and the textures of the monazite. In transect A, the lowest pressure transect in which no rocks contain garnet, allanite starts to break down to monazite ~100 m below the cordierite-in isograd. In transect D, the highest pressure transect in which all rocks contain garnet, allanite begins to break down to form monazite above the garnet isograd. The sample distribution alone in Fig. 2 does not allow a conclusion to be made whether allanite begins to break down within or below the staurolite zone, but the inclusion of allanite and monazite grains in the centre of some staurolite grains, and the breakdown of allanite to monazite downgrade of major phase isograds in all the other transects, suggests that allanite breakdown began prior to the growth of staurolite. This conclusion was also reached by Yang & Pattison (2006) in similar rocks.

The situation is less simple in intermediate-pressure transect B (Fig. 2), in which garnet is sporadically developed in Mn-richer bulk compositions (Table 1). Allanite begins to break down in garnet-free rocks 100–200 m below the andalusite isograd and < 50 m

below the garnet-in isograd (sample 03-OC-08, Fig. 2). However, in a garnet-bearing rock immediately above the garnet-in isograd but below the andalusite isograd (sample 03-OC-07), allanite coexists with garnet in the absence of monazite, suggesting that allanite remained stable above the garnet isograd.

This seemingly contradictory situation may be due to subtle kinetic or bulk compositional controls on the garnet-in and monazite-in reactions that cause them to switch position. The distance between the two samples is < 100 m on the ground, which represents < 10 °C in terms of thermal gradient away from the intrusive contact. Minor differences with respect to some or all of fluid presence and composition, bulk and mineral composition, and effectiveness of chemical communication between modally minor accessory phases, might be sufficient to perturb the onset of reaction by a few degrees and potentially cause the isograds to switch relative position. This situation probably only pertains to transect B because it lies at an intermediate pressure where garnet just begins to become stable.

These details aside, in all three transects monazite starts to form from the breakdown of allanite at or a short distance (< 200 m) downgrade of the major porphyroblast isograds (respectively, for transects A, B and D, cordierite, andalusite and staurolite). The presence or absence of garnet downgrade of the major porphyroblast isograds does not appear to have a significant effect on the position, and therefore onset, of the allanite-to-monazite reaction, a finding also noted by Wing *et al.* (2003). This may be because the allanite-to-monazite reaction involves minerals that are largely independent of those involved in the formation of garnet (compare reactions 6 and 11). A potential exception is allanite, whose stability might be expected to be influenced by garnet growth, but the observations indicate that allanite remains largely euhedral and unreacted even when garnet has formed in the rock (Fig. 4m).

Although garnet formation may not have had any significant effect on the onset of the allanite-to-monazite reaction, it appears to have had an effect on the texture of the monazite that results from the reaction. The conspicuous difference between the garnet-bearing and garnet-absent samples is in the textural development of monazite, with the formation of discrete clusters in garnet-absent samples, and lone grains in garnet-bearing samples. Garnet formation in the Nelson contact aureole occurred via reaction (3), in which muscovite and chlorite break down to form garnet, biotite and fluid. The release of fluids during this reaction may have facilitated increased REE mobility and general length scales of equilibration, allowing the formation of discrete grains randomly distributed throughout the sample matrix, rather than grains spatially associated with allanite as in the garnet-free samples.

Fluid mobilization of REEs has been described in detail by Pan & Fleet (1996). They suggested that REEs, especially LREEs, could be transported as fluoride complexes in high temperature fluids. All of the apatite analysed in this study, from all three transects, is F-rich, with a range between ∼2.8 and 6.7 wt% F (Table 3c). As apatite is inferred to be one of the reactant phases to produce monazite, F would be liberated during the monazite-forming reaction. The F content of micas in the aureole is fairly uniform (∼0.34 wt% for biotite, and 0.14 wt% for muscovite; Pattison & Vogl, 2005), not varying significantly with grade.

Continued growth or reaction of monazite at highest grades in the contact aureole is shown by the rimward enrichment in Th and Y found in monazite from the sillimanite + K-feldspar zone (Fig. 6c,d). This feature is observed in both lone and cluster monazite and is therefore independent of the presence/absence of garnet. At this grade, the monazite rims may have formed in response to the presence of a minor melt component, which is thought by Pattison & Vogl (2005) to closely coincide with the formation of K-feldspar in transect B. The distribution of samples with zoned *v.* unzoned monazite in transect D resembles that in the garnet-bearing transect B sample suite, i.e. restricted to sillimanite grade and higher. Interestingly, xenotime in these high-grade samples is also zoned with respect to HREE, but not at lower grade. If the presence of a small amount of felsic melt produced Th zonation in monazite, it should also have been capable of producing the same effect in other accessory phases.

The presence of higher Th and Y rims in monazite has also been interpreted by others as a response to the presence of melt (e.g. Watt & Harley, 1993) or to melt crystallization (e.g. Spear & Pyle, 2002). Figure 3 of Kohn *et al.* (2005) shows the typical response of monazite composition to ambient *P–T* conditions in pelitic rocks. At low temperatures, during initial monazite growth, the highest Th contents are observed, with a gradual decrease during further monazite growth due to fractionation. Th concentration only increases again during monazite growth during melt crystallization.

Comparison with other studies

The location of the first occurrence of prograde monazite in the lowermost staurolite zone of transect D (Fig. 2b) is similar to reports from previous studies (e.g. Smith & Barreiro, 1990; Kingsbury *et al.*, 1993; Wing *et al.*, 2003; Kohn & Malloy, 2004). In the studies of Pyle & Spear (1999) and Kohn & Malloy (2004), monazite growth was interpreted to occur as part of the reaction that produced staurolite. Growth of staurolite was interpreted to be accompanied by garnet dissolution, with garnet releasing REEs and possibly P to fuel monazite growth. At Nelson, however, monazite growth results from allanite breakdown downgrade of staurolite formation. In addition, staurolite growth in transect D does not appear to have involved significant garnet breakdown (Pattison & Vogl, 2005; Pattison *et al.*, 2005), an observation also

made by Yang & Pattison (2006) in the Black Hills, North Dakota.

Wing *et al.* (2003) suggested that allanite breakdown was triggered by reactions forming any one of a range of aluminosilicate phases (cordierite, staurolite, andalusite, kyanite). That interpretation fits monazite distribution on a gross scale in the Nelson contact aureole, the aluminosilicate phases being cordierite in transect A, andalusite in transect B and staurolite in transect D. In detail, however, monazite appears below these isograds. Thus although there may be a close spatial association between the allanite-to-monazite reaction and the silicate porphyroblast reactions, there does not appear to be a causative relation. The close spatial association suggests that the allanite-to-monazite reaction (11) occurs independently from, but close in temperature to, the breakdown of muscovite + chlorite to either of cordierite, andalusite or staurolite (Fig. 3).

Accessory mineral thermometry

Monazite–xenotime thermometry (Heinrich *et al.*, 1997; Pyle *et al.*, 2001), garnet–xenotime thermometry (Pyle & Spear, 2000) and garnet–monazite thermometry (Pyle *et al.*, 2001) was performed on coexisting accessory phases from all three transects and compared with temperature constraints from silicate phase assemblages (Table 4). Representative analyses of minerals used for thermometry calculations are given in Tables 3a–d.

The silicate temperature estimates are derived from comparison of the reaction isograds in Fig. 2 with the calculated metapelitic phase diagram in Fig. 3, the

latter based on fig. 10c of Pattison & Vogl (2005). These diagrams were calculated using the thermodynamic data set (F.S. Spear, D.R.M. Pattison and J.T. Cheney, unpublished data), described in Pattison *et al.* (2002). Temperatures based on a phase diagram calculated for the same chemical system using the Holland & Powell (1998) thermodynamic database (fig. 10b of Pattison & Vogl, 2005) show the following minimal differences from those listed in Table 4: 10 °C lower for all rocks below the incoming of sillimanite, and 10–20 °C higher for all rocks close to the incoming of Sil + Kfs. Thus, we consider the silicate temperatures to be robust and a good basis for evaluation of the accessory phase thermometry.

Monazite–xenotime thermometry

Monazite–xenotime temperatures generally increase with increasing grade across the aureole. However, the temperatures are consistently lower than those predicted from coexisting silicate assemblages (Table 4), although some of those calculated from the calibration of Heinrich *et al.* (1997) are close to being within error.

Temperature estimates obtained using the natural assemblage-based calibration of Pyle *et al.* (2001) are 90–100 °C lower than those based on the experimentally based Heinrich *et al.* (1997) calibration, a finding also reported by Daniel & Pyle (2006). Assuming monazite and xenotime were in chemical equilibrium, a possible explanation for the temperature differences between the Heinrich *et al.* (1997) and Pyle *et al.* (2001) calibrations is bulk compositional differences between the experimental charges of Heinrich *et al.* (1997) and the natural samples used by Pyle *et al.*

Table 4. Results of accessory mineral thermometry for representative samples from each transect. Averages of multiple analyses are given, including averaged core and rim estimates from garnet-based thermometers. Uncertainties for accessory phase thermometry are 25–30 °C. An activity of water of ~0.8 (Pattison & Vogl, 2005)[a] is assumed for the YAG-mz thermometer of Pyle *et al.* (2001)[b]. Assumed *P* is 3.5 kbar (Pattison & Vogl, 2005). Silicate temperature estimates are from the position of each sample with respect to isograds in Fig. 2, and the temperatures of those isograds from Pattison & Vogl (2005). The silicate temperatures carry an uncertainty of ~25 °C. Representative compositions of minerals used in temperature calculations are given in Table 3. H. *et al* refers to Heinrich *et al.* (1997).

| Location | Sample | Distance from batholith (m) | Silicate assemblage | Silicate T (°C)[a] | Average T (°C) | | grt-xen | | grt-mnz | |
					mnz-xen[b]	mnz-xen (H. *et al.*)	Core	Rim	Core	Rim
Transect A	92-PC-20	650	crd	560	384	483	–	–	–	–
	92-PC-17	420	crd	580	398	496	–	–	–	–
	92-PC-27	80	crd-and	600	469	560	–	–	–	–
Transect B										
Grt absent	92-OC-14	780	and	570	451	544	–	–	–	–
	92-OC-15	730	and	570	462	553	–	–	–	–
	92-OC-19	90	sil	630	488	577	–	–	–	–
Grt bearing	03-OC-06B	1000	grt(e)-chl	≤560	369	469	497	514	409	419
	92-OC-13	900	grt(e)-chl	≤560	333	437	508	505	423	424
	92-OC-17	430	sil-and-grt(e)	610	493	582	543	560	455	493
	03-OC-04	320	sil-and-grt(e)	620	482	571	535	559	452	462
	92-OC-05B	90	siil-grt(l)	630	507	594	569	588	493	526
Transect D	03-CW-04	1340	st-grt(e)	570	454	546	501	525	432	444
	93-CW-23	1130	st-grt(e)	580	474	564	498	554	450	488
	93-CW-10	610	st-and-grt(e)	600	545	628	494	551	456	475
	93-CW-16	270	sil-st-grt(e)	650	494	582	501	573	–	–
Overall mean temperature					453	545	516	547	446	466

(2001). In particular, Gd is significantly higher in the monazite of Heinrich *et al.* (1997). Examination of the data presented in Gratz & Heinrich (1998) reveals that variation in the Gd + Y contents in monazite will produce a change in the location of the monazite limb of the monazite–xenotime miscibility gap in T-X(Y + HREE) space, potentially affecting the resulting temperature calculations.

The significance of the monazite–xenotime temperatures is therefore difficult to determine. Three possible interpretations are: (i) monazite and xenotime underwent continuous chemical exchange and progressively recorded the rise in temperature of the rocks; (ii) monazite retained its composition from the temperature it formed and did not continue to re-equilibrate as temperature rose; or (iii) monazite and xenotime were never in chemical equilibrium, such that the temperatures from monazite–xenotime thermometry are meaningless.

If the 330–545 °C estimates of Pyle *et al.* (2001) are accepted (mean of 453 °C), the only equilibrium interpretation that is possible is the second (ii), implying low-grade (regional metamorphic?) growth of monazite with no subsequent equilibration to higher grade. We do not favour this explanation because our observations indicate that monazite is a contact metamorphic mineral formed only a short distance downgrade of the major phase isograds, and is not present in the regionally metamorphosed rocks well outside the contact aureole.

If the higher 435–630 °C estimates of Heinrich *et al.* (1997) temperatures are accepted, possibilities (i) and (ii) are harder to separate. Most of the temperatures are considerably lower than the silicate temperatures and so argue against continual equilibration with rising temperature, unless the calibration yields results that are systematically in error (too low). The mean of the Heinrich *et al.* temperatures is 545 °C (Table 4), only a little below the temperature of the major phase reactions (~560 °C). Considering that the monazite-in isograd is only a short distance downgrade of the major phase isograds (Fig. 2), this interpretation appears to fit quite well with possibility (ii), although the systematic rise in calculated temperatures with grade suggests this interpretation might be an oversimplification. One possibility is that, following formation of monazite, some degree of equilibration to ambient conditions occurred, but the thermal high from intrusion of the Nelson batholith was not long-lived enough to ensure total re-setting of accessory phase compositions because diffusion rates of REEs were too slow.

The third possibility is that monazite and xenotime were not in chemical equilibrium, recognizing that equilibrium between accessory phases can be difficult to assess (Pyle *et al.*, 2001). These accessory phases are modally minor, fine grained, and widely separated from one another by silicate mineral grains, such that effective chemical communication between them is expected to be difficult. In addition, observations presented earlier suggest that there is no textural or spatial relationship between xenotime and monazite – monazite formation appears to have been independent of xenotime. If monazite and xenotime were not in chemical equilibrium, the monazite–xenotime temperatures are meaningless, and the closeness of some of the temperatures to the silicate temperatures could be coincidental.

Garnet–monazite and garnet–xenotime thermometry

The temperature disparity noted above also pertains to garnet–monazite temperature estimates (444–488 °C in transect D and 419–526 °C in transect B, using garnet rims), again suggesting some or all of calibration problems, disequilibrium between coexisting garnet and monazite, or preservation of the temperature of initial monazite formation at 400–500 °C in rocks that reached > 550 °C. As noted above, we consider this latter possibility to be unlikely based on the closeness of the monazite isograd to the silicate isograds (Fig. 2).

The garnet–xenotime temperatures are 50–100 °C higher than the garnet–monazite temperatures and are thus closer to the silicate temperatures (and Heinrich *et al.* monazite–xenotime temperatures). Possible interpretations of these temperatures are similar to those discussed for the Heinrich *et al.* (1997) monazite–xenotime temperatures.

For both calibrations, garnet core and rim values are given in Table 4, and in each case the core temperature is lower than the rim. This is consistent with, but does not prove, equilibrium between garnet and the accessory phases. At low grade, the core and rim temperatures for both garnet–xenotime and garnet–monazite thermometers are very similar, while at sillimanite-grade they diverge. Given that most if not all garnet growth occurs in the garnet zone (with the exception of narrow rims developed in association with andalusite development in transect D; Pattison & Tinkham, 2005), this could be interpreted to represent equilibration of garnet rim Y compositions with xenotime at the ambient conditions at highest grades. However, the low absolute temperatures are problematic with regard to this interpretation.

Y zoning in garnet

Y zoning in garnet has been used as a monitor of consumption or growth of accessory phases, and of garnet itself. For example, Pyle & Spear (1999) and Kohn & Malloy (2004) argued that the presence of Y annuli in garnet from staurolite zone rocks represents a prograde dissolution-regrowth feature linked to garnet breakdown during staurolite growth and subsequent garnet re-growth. In contrast, Yang & Pattison (2006) interpreted similar-looking Y annuli in staurolite zone rocks from the Black Hills, ND, to be a prograde growth feature that developed due to allanite break-
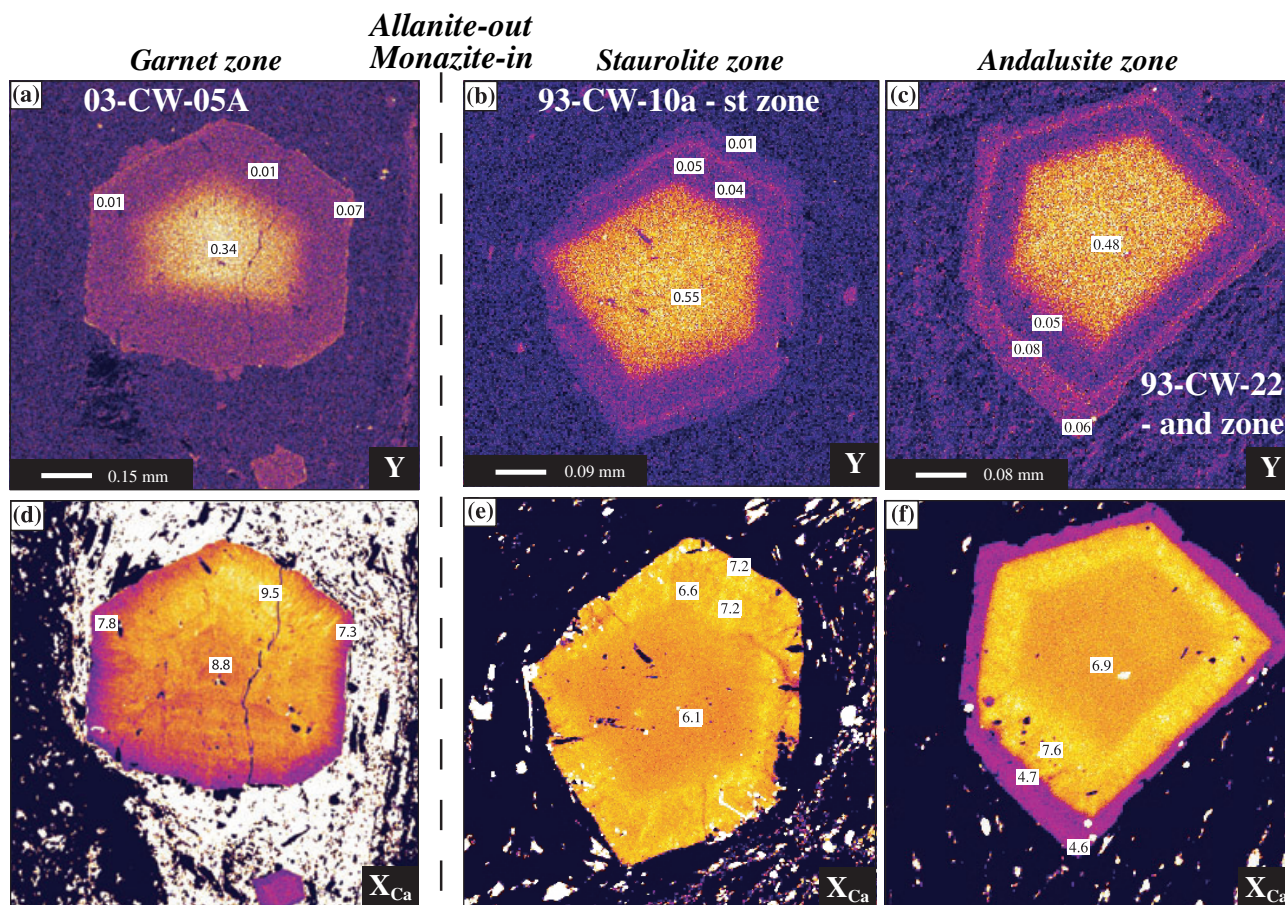
Fig. 8. Element maps of garnet from low to higher grade in transect D. The progression, from left to right in each row, is garnet zone, staurolite zone, andalusite zone (see Fig. 2 for sample locations). The top row of Y maps (a–c) demonstrate the development of a Y annulus in response to allanite breakdown to monazite, with the inner high Y core/low Y rim present prior to allanite breakdown. The lower row of maps (d–f) illustrate Ca zoning. Ca zonation is relatively homogeneous below monazite-in, whereas a zone of higher garnet Ca composition brackets the thin Y annulus. Within the andalusite zone, this higher Ca zone is surrounded by a low Ca rim. Fe, Mg and Mn (not shown here) have simple concentric prograde zonation (Pattison & Tinkham, 2005). In each case the numbers indicate analysis locations, with values of wt% Y_2O_3 and X_{Ca} respectively. Note that $X_{Ca} = Ca/(Ca + Fe + Mg + Mn)$.

down during garnet growth, downgrade of staurolite formation.

Figure 8 shows Ca and Y zoning in garnet from the garnet, staurolite and andalusite zones of transect D that are similar to those described in these other studies. The Ca and Y zoning shows sharp, euhedral outlines, suggesting that it formed via growth rather than dissolution processes. With respect to Ca zoning, there is a core of low(er) Ca composition surrounded by a collar of somewhat higher Ca in garnet from all three zones. In the andalusite zone there is the further development of an abrupt, narrow rim of low-Ca garnet (Fig. 8f), attributed to garnet growth associated with the reaction of staurolite to form andalusite (Pattison & Tinkham, 2005).

With respect to Y, garnet from all three zones shows multiple stages of Y zoning from core to rim; (i) high Y core; (ii) low Y collar; (iii) thin Y annulus. In garnet
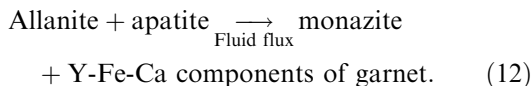
from the staurolite and andalusite zones, there is an additional low Y outer rim. By analogy with the earlier studies, the abrupt transition from the high Y core to low Y collar is most simply interpreted to be due to consumption of xenotime during garnet growth. The obvious difficulty with this interpretation is the presence of xenotime in all samples from sub-garnet grade to sillimanite + K-feldspar grade. An alternative interpretation for the abrupt transition from high Y core to low Y collar, assuming equilibrium with xenotime, is a prograde temperature-dependent zonation, in which the high Y core formed at the lowest metamorphic temperature. In this scenario, the sharp break from core to rim compositions could represent two periods of garnet growth in the garnet zone at different temperatures, separated by a hiatus. A difficulty with this interpretation is the narrowness of the garnet zone, corresponding to a temperature interval of < 20 °C.

Finally, it is possible that the ubiquitous xenotime now present in the matrix of the rocks is of late-stage origin and was therefore not in equilibrium with garnet at the time the low Y collar developed.

The first indication of an Y annulus, outwards of the high Y core and low Y collar, appears in the garnet zone (see Fig. 8a). This garnet coexists with allanite (and the xenotime of uncertain status) in a monazite-absent assemblage; other garnets in the same sample have no Y annuli. In the staurolite and andalusite zones, a euhedral Y annulus is conspicuously developed and is succeeded by an outer low Y rim. As noted above, there is no evidence for significant garnet breakdown accompanying staurolite growth, and no staurolite present whatsoever in the transect B samples whose garnet shows the same zonation patterns. Therefore, we follow the argumentation of Yang & Pattison (2006) in interpreting the Y annulus to be a growth feature developed in association with allanite breakdown in the garnet zone, rather than a dissolution feature related to garnet breakdown to form staurolite. If this is true, the garnet–monazite thermometer (targeting Y compositions from the Y annuli) may potentially be used to constrain the temperature of allanite breakdown to monazite.

In the above interpretations, the status of the ubiquitous xenotime remains unclear, a problem that presented itself earlier in the interpretation of the monazite–xenotime and garnet–xenotime thermometry and in the interpretation of the transition from high Y core to low Y collar in garnet. Xenotime appears to be coarser grained at higher grade, but otherwise its distribution and texture seems more or less indifferent to the distribution and texture of other minerals in the rock.

Assuming our interpretation that Y annuli formation in the Nelson aureole garnet was associated with allanite breakdown is correct, the following reaction is considered for monazite formation in transects B (garnet-bearing) and D:

$$\text{Allanite} + \text{apatite} \xrightarrow[\text{Fluid flux}]{} \text{monazite}$$
$$+ \text{ Y-Fe-Ca components of garnet.} \qquad (12)$$

In this case, the Fe component of garnet replaces magnetite from reaction (11), and the Ca component of garnet replaces anorthite in plagioclase. There is no indication for this process in the Ca or Fe zoning of garnet, perhaps because the small amounts of both Fe and Ca released in this reaction are distributed amongst modally abundant garnet, biotite and plagioclase, leaving no significant geochemical signature.

Other phases also exhibit trace element zonation that may be related to the presence of, or coexistence with, garnet. Although not true for every case, allanite may be zoned in samples where it coexists with garnet, such as 03-CW-05A (Fig. 9a). In this sample, the M-HREEs and Y in allanite decrease from core to rim,
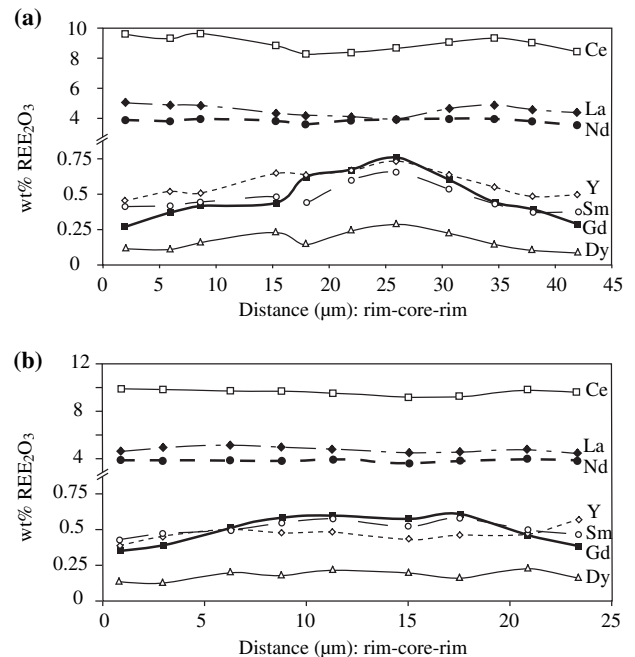

Fig. 9. (a) Traverse of allanite coexisting with garnet, from sample 03-CW-05A. (b) Traverse of allanite from garnet-absent sample 03-CW-08B. Note that the error on these rare earth element oxide analyses is no more than 0.02 wt%, and so the observed zonation is real.

suggesting that garnet growth resulted in the depletion of HREEs and especially Y in coexisting allanite rims. In garnet-absent samples, HREE zonation is similar, however the Y zonation remains nearly constant across the entire grain (Fig. 9b). Apatite coexisting with garnet, such as that from transects B and D, shows the same pattern of rimward HREE and Y depletion.

GEOCHRONOLOGY

Chemical dating was performed on a range of samples from different transects in the Nelson contact aureole, using the Jeol JXA-8200 electron microprobe at the University of Calgary. The aim of this exercise was to determine whether the monazite described in this study gave the same age as the Nelson Batholith (158–172 Ma; Sevigny & Parrish, 1993; Ghosh, 1995), as is predicted from its contact metamorphic origin. Most monazite was too small for more than one analysis per grain, with few monazite grains larger than 20 μm. Composition of the Nelson monazite generally falls within a limited range (Table 3a), except for Th (and Y). ThO_2 content varies from 1.02 wt% to as high as 16.08 wt% due to the presence of high Th cores and rimward Th zonation observed in some grains. UO_2 is less varied, ranging from 0.09 to 1.27 wt%, with a mean concentration of 0.34 wt%. In such young monazite, PbO is at
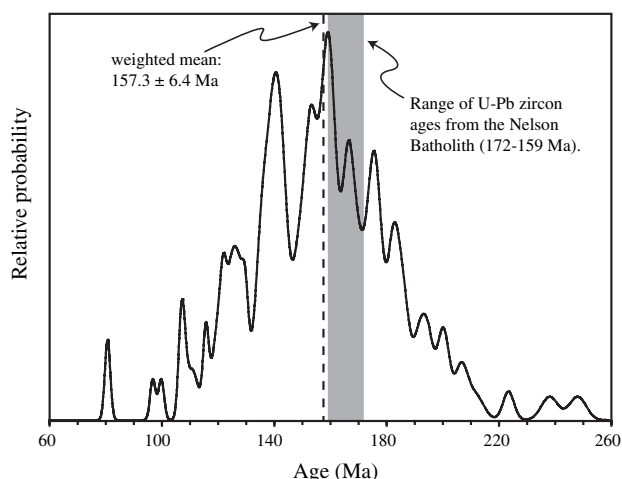
Fig. 10. Histogram of chemical monazite ages for Nelson contact aureole pelites. The weighted mean for the main population is 157 ± 6 (2σ error, MSWD = 64, n = 97). This age is within error of the isotopic U-Pb age of zircon from the Nelson Batholith (159–172 Ma; Sevigny & Parrish, 1993; Ghosh, 1995).

quite low concentrations, and falls in the range 200–980 p.p.m. The mean PbO is 388 p.p.m. Note that this is a mixture of radiogenic and common Pb, which are indistinguishable by electron probe. Common Pb (^{204}Pb) will impart bias to the derived ages.

Geochronology results are given in Supplementary Appendix S1. As a whole, the data describe a single age of c. 160–140 Ma, however in detail it may be possible to define two discrete populations, one at c. 157 Ma and the other at c. 140 Ma (Fig. 10). The total range of ages is from 248 to 81 Ma, with the scatter to younger ages related to the very low Pb concentrations in these young monazites creating a significant amount of error related to detection limits during analysis (estimated to be 200 p.p.m. for Pb). For these reasons, it would be unwise to ascribe too much weight to the apparent complexity of the age data in Fig. 10. If the broader population is treated as one peak, a weighted mean returns an age of 157.3 ± 6.4 Ma (2σ), which is close to, and within error of, the isotopic U-Pb zircon ages of Sevigny & Parrish (1993) and Ghosh (1995). The large MSWD (64) is related to the large range and errors inherent in such a young population using this technique. However, from this data set, it can be seen that the age of Nelson aureole monazite is consistent with their interpreted contact metamorphic origin.

SUMMARY AND CONCLUSIONS

Monazite formation in the Nelson contact aureole is the result of allanite breakdown close to, but below, the major silicate isograds (cordierite-in, andalusite-in and staurolite-in), and is not triggered by these reactions. This is an alternative interpretation to that developed by Pyle & Spear (1999, 2003), Wing *et al.* (2003), and Kohn & Malloy (2004) in which major

phase reactions involving andalusite, cordierite, staurolite or garnet play a direct role in monazite formation.

Early garnet growth does not seem to influence the onset of the allanite-to-monazite reaction (as also concluded by Wing *et al.*, 2003). The allanite-to-monazite reaction starts < 200 m below the main phase isograds regardless of the presence or absence of garnet, suggesting that the reaction is thermally activated and operates independently from the silicate reactions at a temperature a little below the breakdown of muscovite and chlorite to cordierite, andalusite or staurolite. However, the presence or absence of garnet appears to have a significant effect on monazite texture, which may be related to fluid fluxing during breakdown of chlorite and muscovite and perhaps apatite, to form garnet.

Accessory phase thermometry is difficult to interpret in the Nelson contact aureole due to the disparity of temperature estimates from different mineral pairs (monazite–xenotime, garnet–xenotime, garnet–monazite) and different calibrations of the same mineral pair (e.g. Pyle *et al.* (2001) *v.* Heinrich *et al.* (1997) calibrations of the monazite–xenotime pair). This disparity may in part be due to lack of equilibration between phases. The differences in monazite–xenotime thermometry may be partly a function of differences in mineral composition involved in each calibration.

Euhedral Y zoning in garnet porphyroblasts is typified by a core-rim progression involving a high Y core, transitioning to a low Y collar, and a moderate Y annulus. The traditional interpretation of the transition from the high Y core to low Y collar being due to xenotime consumption during garnet growth in the garnet zone (e.g. Pyle & Spear, 1999; Yang & Pattison, 2006) is compromised by the ubiquitous presence of xenotime in the matrix of the rocks. The Y annulus is ascribed to allanite breakdown to monazite during subsequent garnet growth in the garnet zone, rather than to garnet breakdown in association with staurolite formation as suggested in other studies.

U-Pb geochronology of Nelson monazite by electron microprobe returns a weighted mean age of 157.3 ± 6.4 Ma (2σ). This is in agreement with previous isotopic studies, and supports a contact metamorphic origin for the monazite.

REFERENCES

Archibald, D. A., Glover, J. K., Price, R. A., Farrar, E. & Carmichael, D. M., 1983. Geochronology and tectonic implications of magmatism and metamorphism, southern Kootenay Arc and neighbouring regions, southeastern British Columbia. I. Jurassic to Cretaceous. *Canadian Journal of Earth Sciences*, **20**, 1981–1913.

Archibald, D. A., Krogh, T. E., Armstrong, R. L. & Farrar, E., 1984. Geochronology and tectonic implications of magmatism and metamorphism, southern Kootenay Arc and neighbouring regions, southeastern British Columbia. II. Mid-Cretaceous to Eocene. *Canadian Journal of Earth Sciences*, **21**, 567–583.

Carr, S. D., Parrish, R. R. & Brown, R. L., 1987. Eocene structural development of the Valhalla Complex, southeastern British Columbia. *Tectonics*, **6**, 175–196.

Daniel, C. G. & Pyle, J. M., 2006. Monazite-xenotime thermometry and Al_2SiO_5 reaction textures in the Picuris Range, Northern New Mexico, USA: new evidence for a 1450–1400 Ma orogenic event. *Journal of Petrology*, **47**, 97–118.

Degeling, H., Eggins, S. & Ellis, D. J., 2001. Zr budgets for metamorphic reactions and the formation of zircon from garnet breakdown. *Mineralogical Magazine*, **65**, 761–770.

Fletcher, I. R., Rasmussen, B. & McNaughton, N. J., 2000. SHRIMP U-Pb geochronology of authigenic xenotime and its potential for dating sedimentary basins. *Australian Journal of Earth Sciences*, **47**, 845–859.

Foster, G., Gibson, H. D., Parrish, R., Horstwood, M., Fraser, J. & Tindle, A., 2002. Textural, chemical and isotopic insights into the nature and behaviour of metamorphic monazite. *Chemical Geology*, **191**, 183–207.

Fraser, G., Ellis, D. & Eggins, S., 1997. Zirconium abundance in granulite-facies minerals, with implications for zircon geochronology in high-grade rocks. *Geology*, **25**, 607–610.

Fraser, G. L., Pattison, D. R. M. & Heaman, L. M., 2004. Age of the Ballachulish and Glencoe Igneous Complexes (Scottish Highlands), and paragenesis of zircon, monazite and baddeleyite in the Ballachulish Aureole. *Journal of the Geological Society of London*, **161**, 447–462.

Fyles, J. T., 1967. Geology of the Ainsworth-Kaslo area, British Columbia. *British Columbia Department of Mines Bulletin*, **53**.

Ghosh, D. K., 1995. U-Pb geochronology of Jurassic to early Tertiary granitic intrusives from the Nelson-Castlegar area, southeastern British Columbia, Canada. *Canadian Journal of Earth Sciences*, **32**, 1668–1680.

Gratz, R. & Heinrich, W., 1998. Monazite-xenotime thermometry, III: Experimental calibration of the partitioning of Gd between monazite and xenotime. *European Journal of Mineralogy*, **10**, 579–588.

Heinrich, W., Andrehs, G. & Franz, G., 1997. Monazite-xenotime miscibility gap thermometry; 1, An empirical calibration. *Journal of Metamorphic Geology*, **15**, 3–16.

Holland, T. J. B. & Powell, R., 1998. An internally consistent thermodynamic data set for phases of petrological interest. *Journal of Metamorphic Geology*, **16**, 309–344.

Kingsbury, J. A., Miller, C. F., Wooden, J. L. & Harrison, T. M., 1993. Monazite paragenesis and U-Pb systematics in rocks of the eastern Mojave Desert, California, U.S.A.: implications for thermochronometry. *Chemical Geology*, **110**, 147–167.

Kohn, M. J. & Malloy, M. A., 2004. Formation of monazite via prograde metamorphic reactions among common silicates: implications for age determinations. *Geochimica et Cosmochimica Acta*, **68**, 101–113.

Kohn, M. J., Wieland, M. S., Parkinson, C. D. & Upreti, B. N., 2005. Five generations of monazite in Langtang gneisses: implications for chronology of the Himalayan metamorphic core. *Journal of Metamorphic Geology*, **23**, 399–406.

Little, H. W., 1960. Nelson map area, west half, British Columbia. *Geological Survey of Canada Memoir*, **308**.

Nguyen, K. K., Sinclair, A. J. & Libby, W. G., 1968. Age of the northern part of the Nelson batholith. *Canadian Journal of Earth Sciences*, **5**, 955–957.

Pan, Y. & Fleet, M. E., 1996. Rare earth element mobility during prograde granulite facies metamorphism: significance of fluorine. *Contributions to Mineralogy and Petrology*, **123**, 251–262.

Parrish, R. R., Carr, S. D. & Parkinson, D. L., 1988. Eocene extensional tectonics and the geochronology of the southern Omineca Belt, British Columbia. *Tectonics*, **2**, 181–212.

Pattison, D. R. M. & Tinkham, D. K., 2005. Garnet and staurolite behaviour in the Nelson aureole, BC: implications for phase equilibrium modelling and reaction kinetics. *Geological Society of America*, Abstracts with Program, **37**, p. 53.

Pattison, D. R. M. & Vogl, J. J., 2005. Contrasting sequences of metapelitic mineral-assemblages in the aureole of the tilted Nelson Batholith, British Columbia: implications for phase equilibria and pressure determination in andalusite-sillimanite type settings. *Canadian Mineralogist*, **43**, 51–88.

Pattison, D. R. M., Spear, F. S., DeBuhr, C. L., Cheney, J. T. & Guidotti, C. V., 2002. Thermodynamic modelling of the reaction Muscovite + Cordierite = Al_2SiO_5 + Biotite + Quartz + H_2O: constraints from natural assemblages and implications for the metapelitic petrogenetic grid. *Journal of Metamorphic Geology*, **20**, 99–118.

Pattison, D. R. M., Tinkham, D. K. & Yang, P., 2005. Unreactivity of garnet in low pressure metapelites. *15th Goldschmidt Conference* (Moscow, Idaho), May 20–25, 2005.

Pyle, J. M. & Spear, F. S., 1999. Yttrium zoning in garnet: coupling of major and accessory phases during metamorphic reactions. *Geological Materials Research*, **1**, 1–49.

Pyle, J. M. & Spear, F. S., 2000. An empirical garnet (YAG)-xenotime thermometer. *Contributions to Mineralogy and Petrology*, **138**, 51–58.

Pyle, J. M. & Spear, F. S., 2003. Four generations of accessory-phase growth in low-pressure migmatites from SW New Hampshire. *American Mineralogist*, **88**, 338–351.

Pyle, J. M., Spear, F. S., Rudnick, R. L. & McDonough, W. F., 2001. Monazite-xenotime-Garnet equilibrium in metapelites and a new monazite-garnet thermometer. *Journal of Petrology*, **11**, 2083–2107.

Rasmussen, B., 1996. Early diagenetic REE phosphate minerals (florencite, gorceixite, crandellite and xenotime) in marine sandstones: a major sink for oceanic phosphorous. *American Journal of Science*, **296**, 601–632.

Rasmussen, B., Buick, R. & Taylor, W. R., 1998. Removal of oceanic REE by authigenic precipitation of phosphatic minerals. *Earth and Planetary Science Letters*, **164**, 135–149.

Sevigny, J. H. & Parrish, R. R., 1993. Age and origin of Late Jurassic and Paleocene granitoids, Nelson Batholith, southern British Columbia. *Canadian Journal of Earth Sciences*, **30**, 2305–2314.

Smith, H. A. & Barreiro, B., 1990. Monazite U-Pb dating of staurolite grade metamorphism in pelitic schists. *Contributions to Mineralogy and Petrology*, **105**, 602–615.

Spear, F. S. & Pyle, J. M., 2002. Apatite, monazite and xenotime in metamorphic rocks. *Reviews in Mineralogy*, **48**, 293–335.

Sweetkind, D. S. & Duncan, I. J., 1989. Fission-track evidence for Cenozoic uplift of the Nelson batholith, southeastern British Columbia. *Canadian Journal of Earth Sciences*, **26**, 1944–1952.

Tomkins, H. S., Williams, I. S. & Ellis, D. J., 2005. In situ U-Pb dating of zircon formed from retrograde garnet breakdown during decompression in Rogaland, SW Norway. *Journal of Metamorphic Geology*, **23**, 201–215.

Watt, G. R. & Harley, S. L., 1993. Accessory phase controls on the geochemistry of crustal melts and restites produced during contact and regional metamorphism of pelites: petrology and geochronology. *Contributions to Mineralogy and Petrology*, **114**, 550–566.

Wing, B. A., Ferry, J. M. & Harrison, T. M., 2003. Prograde destruction and formation of monazite and allanite during contact and regional metamorphism of pelites: petrology and geochronology. *Contributions to Mineralogy and Petrology*, **145,** 228–250.

Yang, P. & Pattison, D. R. M., 2006. Genesis of monazite and Y-zoning in garnet from the Black Hills, South Dakota. *Lithos*, **88,** 233–253.

SUPPLEMENTARY MATERIAL

The following supplementary material is available for this article online from http://www.blackwell-synergy.com:

Appendix S1. Results of chemical dating analyses for Nelson contact aureole monazites.